RESEARCH ARTICLE

Key Points:
- New satellite radar interferometry identifies accelerating uplift pulses at Aluto volcano, Ethiopia
- Deformation source models suggest inflation events are linked to magmatic or fluid intrusion at 5 km
- CO_2-$\delta^{13}C$ reveals connected magmatic-hydrothermal system that could account for subsequent deflation

Supporting Information:
- Supporting Information S1
- Table S1

Correspondence to:
W. Hutchison,
wh39@st-andrews.ac.uk

Causes of unrest at silicic calderas in the East African Rift: New constraints from InSAR and soil-gas chemistry at Aluto volcano, Ethiopia

William Hutchison[1,2], Juliet Biggs[3], Tamsin A. Mather[1], David M. Pyle[1], Elias Lewi[4], Gezahegn Yirgu[5], Stefano Caliro[6], Giovanni Chiodini[6], Laura E. Clor[7], and Tobias P. Fischer[8]

[1]COMET, Department of Earth Sciences, University of Oxford, Oxford, UK, [2]Now at Department of Earth and Environmental Sciences, University of St. Andrews, UK, [3]COMET, School of Earth Sciences, University of Bristol, Wills Memorial Building, Bristol, UK, [4]IGSSA, Addis Ababa University, Addis Ababa, Ethiopia, [5]School of Earth Sciences, Addis Ababa University, Addis Ababa, Ethiopia, [6]Istituto Nazionale di Geofisica e Vulcanologia, Osservatorio Vesuviano, Napoli, Italy, [7]U.S. Geological Survey, Menlo Park, California, USA, [8]Department of Earth and Planetary Sciences, MSC03 2040, New Mexico, USA

Abstract Restless silicic calderas present major geological hazards, and yet many also host significant untapped geothermal resources. In East Africa, this poses a major challenge, although the calderas are largely unmonitored their geothermal resources could provide substantial economic benefits to the region. Understanding what causes unrest at these volcanoes is vital for weighing up the opportunities against the potential risks. Here we bring together new field and remote sensing observations to evaluate causes of ground deformation at Aluto, a restless silicic volcano located in the Main Ethiopian Rift (MER). Interferometric Synthetic Aperture Radar (InSAR) data reveal the temporal and spatial characteristics of a ground deformation episode that took place between 2008 and 2010. Deformation time series reveal pulses of accelerating uplift that transition to gradual long-term subsidence, and analytical models support inflation source depths of ~5 km. Gases escaping along the major fault zone of Aluto show high CO_2 flux, and a clear magmatic carbon signature (CO_2-$\delta^{13}C$ of $-4.2‰$ to $-4.5‰$). This provides compelling evidence that the magmatic and hydrothermal reservoirs of the complex are physically connected. We suggest that a coupled magmatic-hydrothermal system can explain the uplift-subsidence signals. We hypothesize that magmatic fluid injection and/or intrusion in the cap of the magmatic reservoir drives edifice-wide inflation while subsequent deflation is related to magmatic degassing and depressurization of the hydrothermal system. These new constraints on the plumbing of Aluto yield important insights into the behavior of rift volcanic systems and will be crucial for interpreting future patterns of unrest.

1. Introduction

Caldera complexes are characterized by regular unrest events (i.e., elevated seismicity, deformation and gas emissions) and infrequent large eruptions [*Dvorak and Dzurisin*, 1997; *Biggs et al.*, 2014], making them some of the most dangerous and unpredictable volcanic systems on Earth [*Acocella et al.*, 2015]. Understanding what causes unrest at these systems is vital for deciphering the behavior of the volcano during intereruptive periods and forecasting eruptions [*Parks et al.*, 2012, 2015]. The fundamental challenge for volcanologists is to link the unrest observed at the surface to an unseen physical process taking place at depth. This requires knowledge of the location and geometry of the magmatic and hydrothermal reservoirs as well as their connections and interactions. Often a high-temporal resolution monitoring effort, combining geophysical and geochemical observations, is required to elucidate this [e.g., *Chiodini et al.*, 2010, 2012, 2015a].

The East African Rift System (EARS) hosts a number of large (>10 km diameter) silicic caldera systems [*Mohr et al.*, 1980; *Acocella et al.*, 2003; *Rampey et al.*, 2010, 2014; *Robertson et al.*, 2015]. Unlike similar-sized volcanoes in developed nations, none of the EARS calderas are permanently monitored and in almost all cases knowledge of the frequency and magnitude of past eruptions is extremely limited [*Brown et al.*, 2015]. Without this information, volcanologists are reliant on regional satellite remote sensing surveys to detect caldera unrest. In the EARS, *Biggs et al.* [2009a, 2011, 2016] used Interferometric Synthetic Aperture Radar (InSAR) to
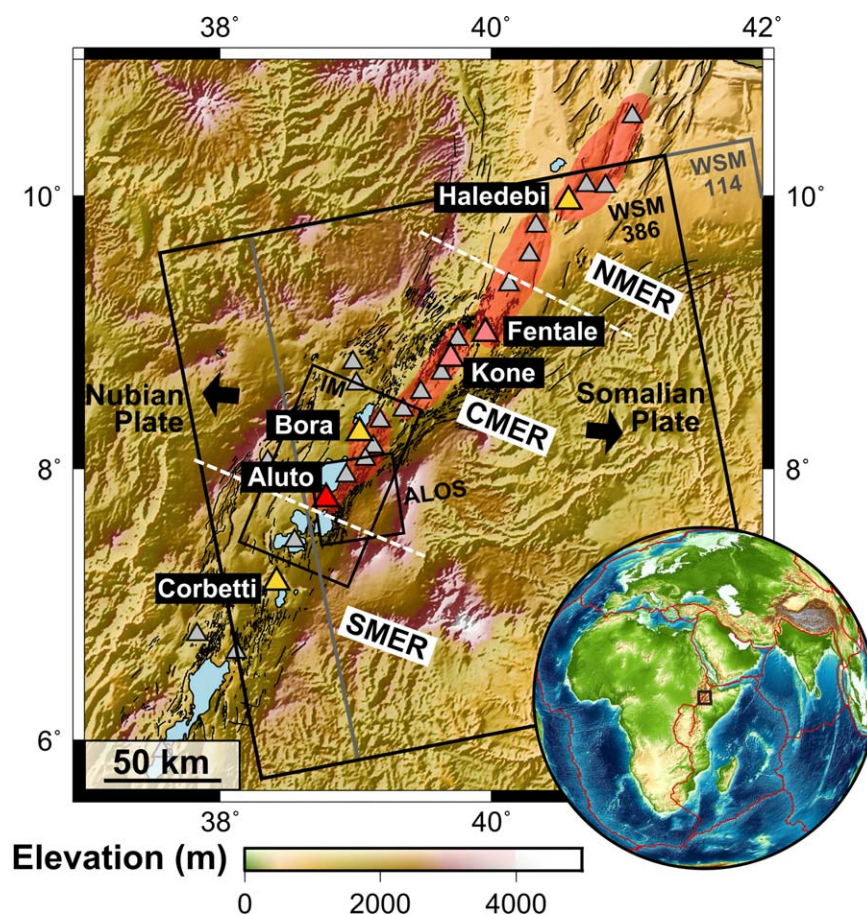
Figure 1. Shaded relief map of the Main Ethiopian Rift (MER). Holocene volcanic centers are shown as triangles [after *Siebert and Simkin*, 2002]. Aluto volcano, the focus of this study, is shown in red, other deforming volcanoes [after *Biggs et al.*, 2011] are shown in yellow, and those that have undergone historical eruptions are shown in pink [see *Rampey et al.*, 2010 and references therein]. Note that ground deformation has not been detected at volcanoes that have undergone historical eruptions [*Biggs et al.*, 2011]. Fault structures [modified after *Agostini et al.*, 2011] are shown as black lines. The red shaded areas mark the extent of volcanic segments of the MER [cf. *Ebinger and Casey*, 2001]. Black arrows show the extension direction after *Saria et al.* [2014]. Rectangles indicate the coverage of the four SAR data sets used in this study. WSM: Envisat Wide Swath Mode and IM: Envisat Image Mode.

successfully identify unrest events at several major calderas in Kenya (Paka, Longonot, Silali, Menegai, and Suswa volcanoes) and Ethiopia (Aluto and Corbetti volcanoes, Figure 1).

Many of the restless calderas identified by *Biggs et al.* [2009a, 2011, 2016] also host large hydrothermal systems and thus recoverable geothermal energy resources. Although the geothermal industry is still at an early stage in the EARS it could offer significant economic benefits for the developing nations that host these resources [e.g., Ethiopia, Kenya and Tanzania, *Kebede*, 2012; *Younger*, 2014], and an emerging issue is how to balance the competing demands for geothermal infrastructure development with the risks that these poorly studied, unmonitored volcanic systems pose.

Knowledge of the subsurface volcanic processes that cause unrest at these calderas is essential for assessing hazards and understanding the potential risks. Here we combine geodetic observations of ground displacement with geochemical constraints from degassing to evaluate magmatic-hydrothermal interactions at Aluto volcano, Ethiopia (Figure 1). Aluto presents a suitable target for this study because it shows signs of unrest (identified by InSAR) [*Biggs et al.*, 2011], and hosts a major geothermal field which has been and is being drilled, allowing us to place constraints on the subsurface structure. We undertake an expanded analysis of InSAR data to evaluate spatiotemporal patterns of deformation and establish constraints on the depths and volume of fluids involved in the unrest events. We also report new soil-gas chemical data that help explore physical connections between the magmatic and geothermal reservoirs of Aluto. Together, these techniques shed light on the subsurface

of a restless caldera system, and reveal important coupling between magmatic and hydrothermal processes that could be widely applicable throughout the EARS.

2. Geological Setting

The ~500 km long Main Ethiopian Rift (MER, Figure 1) accommodates extension between the Nubian and Somalian Plates and constitutes the northernmost segment of the EARS [*Corti*, 2009]. The MER is often considered to be the type example of a continental rift [*Ebinger*, 2005] and is traditionally separated into three Northern, Central, and Southern sectors [*Corti*, 2009]. These rift sectors developed asynchronously and display clear along-axis variations in fault architecture, magmatic processes, and modification of the crust [see *Keir et al.*, 2015, and references therein]. Rift maturity increases northward along the MER toward Afar, where the overall physiology changes from continental rifting to incipient oceanic spreading [*Beutel et al.*, 2010; *Ebinger et al.*, 2010; *Ferguson et al.*, 2013]. The MER is an ideal setting to develop models of continental rift evolution and it has been demonstrated that early stages of extension are accommodated by deformation on large boundary faults and that over time magma-assisted rifting becomes increasingly dominant with extension narrowing toward the rift axis [*Ebinger*, 2005; *Corti*, 2009]. The major transition in rifting dynamics, from boundary fault-dominated extension to localized axial volcanic segments (Figure 1), appears to take place in the Northern and Central MER (NMER and CMER) at around 3–1.6 Ma [*Boccaletti et al.*, 1998; *Le Turdu et al.*, 1999; *Ebinger and Casey*, 2001], while in the Southern MER active deformation remains largely fault-controlled [*Hayward and Ebinger*, 1996; *Corti et al.*, 2013; *Philippon et al.*, 2014].

Aluto is a silicic peralkaline volcano and is located in the CMER ~100 km south of Addis Ababa. It is bounded and dissected by NNE-SSW-trending faults (Figure 2a), commonly referred to as Wonji Fault Belt [e.g., *Acocella et al.*, 2003; *Agostini et al.*, 2011; *Hutchison et al.*, 2015]. The complex has been targeted for geothermal development and eight exploration wells were drilled during the 1980s (LA-1–LA-8; Figure 2a) with the deepest reaching ~2500 m below the surface [*Gianelli and Teklemariam*, 1993; *Gizaw*, 1993; *Teklemariam et al.*, 1996]. Of the eight wells drilled, only two (LA-3 and LA-6) are productive to date. *Hutchison et al.* [2015] identified two major structural features at the surface of the Aluto, a 500 m long fault, referred to as the Artu Jawe fault zone (AJFZ), which is aligned with local NNE-SSW-trending Wonji structures, and a 2500 m long remnant of a caldera rim on the east of the complex. Deep well correlations suggest that faulting preceded volcanic activity at Aluto [*Hutchison et al.*, 2015] and that the silicic complex was initially built up as a low-relief shield before undergoing a period of caldera collapse. Significant post-caldera activity then took place at Aluto progressively infilling the caldera and the most recent eruptions, which include pumice fall, pyroclastic density current and lava flow units, have exploited structural weaknesses created by the pre-existing volcanic and tectonic structures (e.g., the AJFZ). Diffuse volcanic degassing also takes place at a number of sites across the volcano and it is evident that the pre-existing structures also dictate gas and hydrothermal fluid ascent to the surface. Aluto has undergone multiple uplift and subsidence events since 2003 [*Biggs et al.*, 2011]. The cause of these unrest events is the focus of this study (section 7) and was also the topic of a recent magnetotelluric survey by *Samrock et al.* [2015] at Aluto.

3. Methods

3.1. InSAR Data and Processing

InSAR is a geodetic technique that measures phase difference between two Synthetic Aperture Radar acquisitions [e.g., *Simons and Rosen*, 2007, and references therein]. The technique has been successfully applied in many volcanic settings, including rift zones [e.g., Iceland: *Sigmundsson et al.*, 2010, 2014 and East Africa: *Wright et al.*, 2006; *Biggs et al.*, 2009a, 2011, 2016; *Wauthier et al.*, 2012, 2013]. Here we use four sets of SAR data acquired by Envisat and ALOS satellites from 2002 to 2012 (summarized in Table 1, and in Figure 1 where swath coverage is shown) and have generated ~100 interferograms in total.

Interferograms for Envisat Image Mode (IM) and ALOS data were generated using the Repeat Orbit Processing software (ROI_PAC) [*Rosen et al.*, 2004]. For the Envisat Wide Swath Mode (WSM) data we processed the interferograms using Gamma software [*Wegmüller and Werner*, 1997]. For all data sets, we removed the topographic contribution using an identical 90 m SRTM DEM. The Envisat WSM data has the lowest spatial resolution of SAR data sets included in this study (150 m) and so a 90 m DEM is sufficient to ensure that this data is not downsampled. It is also important to note that although a 2 m lidar DEM is available for Aluto
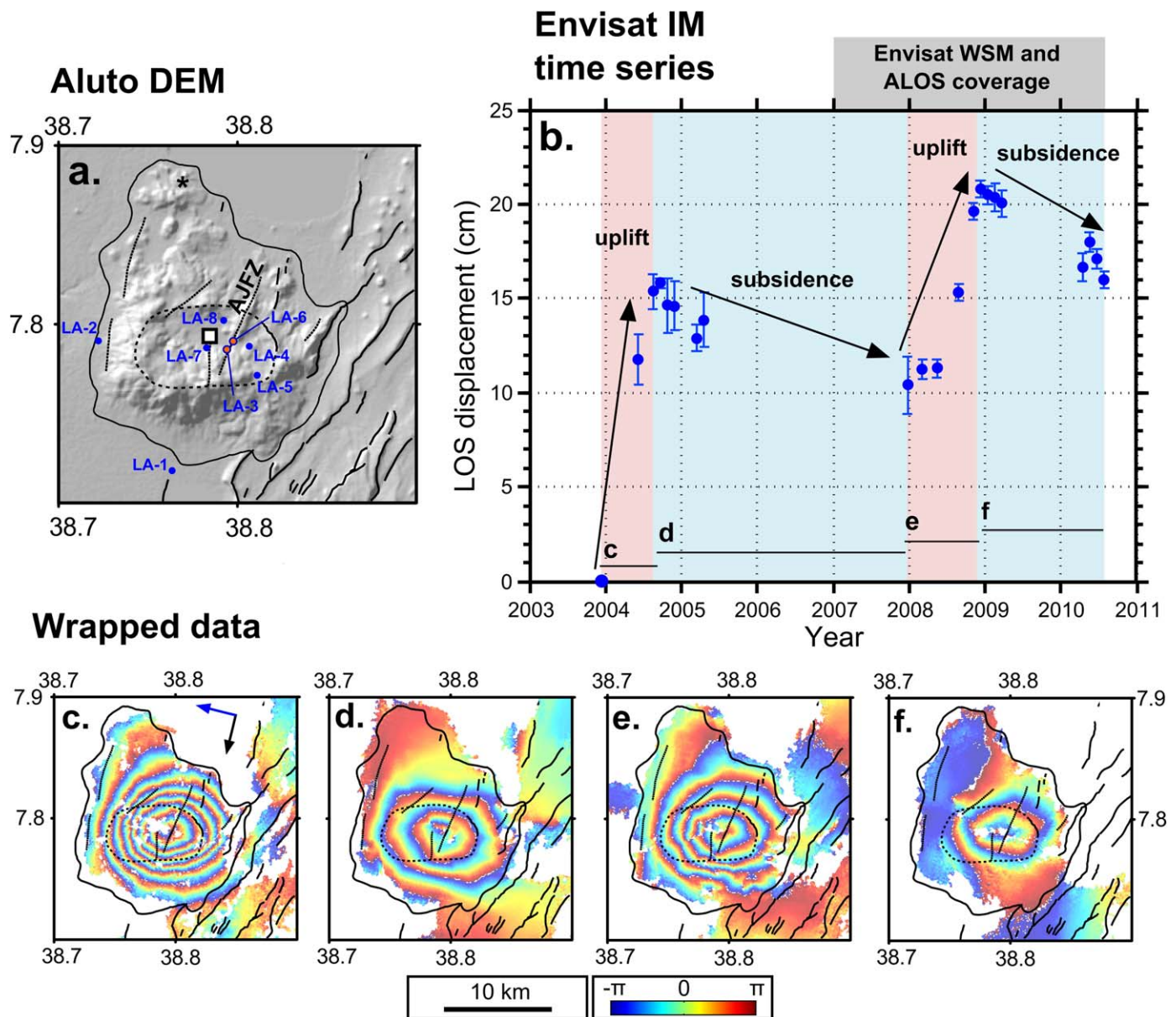
Figure 2. Results from Envisat IM time series. (a) Hillshade DEM of Aluto volcano. Black outline marks the extent of volcanic deposits, dashed line delineates the hypothesized ring fracture beneath Aluto [after *Hutchison et al.*, 2015], and NE-SW trending lines indicate tectonic faults [after *Agostini et al.*, 2011]. The major tectonic fault that dissects Aluto is referred to as the Artu Jawe fault zone (AJFZ) and is labeled in the figure. (b) Envisat IM line of sight (LOS) displacement time series. The black asterisk (in Figure 2a) locates the reference pixel while the white square (in Figure 2a) contains pixels used in the time series analysis. (c)–(f) Example interferograms that correspond to the time period shown in the time series (labeled as black horizontal lines in Figure 2b). Colors in Figures 2c–2f show ground displacement in the direction from the ground to the satellite and each color fringe represents 2.83 cm of LOS displacement. The red arrow indicates orientation of satellite orbit, and the blue arrow indicates the look direction of the satellite.

[*Hutchison et al.*, 2015] it does not cover the non-deforming areas away from the main edifice and therefore cannot be used to generate reliable displacement time series (section 3.2). Linear ramps were found in the phase data for several interferograms and were likely caused by inaccuracies in the satellite orbital positions. In these cases, orbital ramps were sampled, modeled (fitting a linear or quadratic surface), and then subtracted from the interferogram [e.g., *Ebmeier et al.*, 2010]. Topographically correlated atmospheric delay errors (i.e., water vapor effects) were very minor because the relief over the Aluto complex is low (<700 m).

3.2. Displacement Time Series and Components of Ground Motion
InSAR measures displacement along a single line of sight (LOS). For each track, we constructed a LOS deformation time series by using a linear least squares inversion of the displacements for each interferogram to

Table 1. Summary of Satellite Data Sets Used in the Study

Instrument	Operation mode	Operational period	Wavelength (cm)	Repeat interval (days)	Swath (km)	Orbital node	Tracks processed	Number of scenes	Heading angle (°)	Look angle (°)
Envisat (ESA)	Image mode (IM)	2002–2012	5.66 (C-band)	35	58–100	Descending	321	25	−167	22
	Wide Swath Mode (WSM)	2007–2012[a]	5.66 (C-band)	35	∼400	Ascending	386 and 114 (both IS1 subswath)	32 and 34	−12	18 and 24
ALOS (JAXA)	PALSAR	2007–2011	23.6 (L-Band)	46	70	Ascending	605	13	−12	40

Note: The majority of our data was acquired by the European Space Agency's (ESA) Envisat satellite. In this study, we use Envisat data collected in Image Mode (IM) and Wide Swath Mode (WSM). IM is Envisat's conventional operation mode. The Scanning Synthetic Aperture Radar (ScanSAR) technique of the Envisat ASAR instrument, hereafter referred to as the WSM mode, permits radar observations with a much larger swath (∼400 km) but with a reduced spatial resolution compared to IM. WSM covers the extended area by using five different overlapping antenna beams (subswaths) [*Moore et al.*, 1981]. We also processed Phased Array type L-band Synthetic Aperture Radar (PALSAR) data from the Japanese Aerospace Exploration Agency (JAXA) ALOS satellite.

[a]Data covering the Ethiopian Rift extends until December 2008.

find incremental displacements between the acquisition dates [e.g., *Lundgren et al.*, 2001; *Berardino et al.*, 2002; *Biggs et al.*, 2010]. Each displacement time series (Figures 2–5) is referenced to a pixel (asterisk, Figure 2a) located ∼5 km north-west of the main edifice of Aluto. This reference locality was coherent throughout the survey period for all data sets and is assumed not to be deforming (there is no evidence of recent fault scarps within the vicinity of this site). We found that referencing the time series to coherent regions east of the main edifice produced very similar time series results to those shown in Figures 2–5. Uncertainties in the time series were estimated using a Monte Carlo approach, where randomly generated noise of mean amplitude 1 cm was added to every pixel in each interferogram before inversion, neglecting the effects of spatial correlation [*Ebmeier et al.*, 2013a]. Error bars in LOS displacement time series are variable and reflect how well each acquisition date is linked to the network of interferograms [e.g., *Ebmeier et al.*, 2013b].

The interferograms processed for each orbital track were acquired from different satellite viewing geometries (Table 1, note differences in heading and look angles). Using LOS displacement measurements made from different satellite look directions, it is possible to combine the images and resolve the horizontal (U_x) and vertical (U_z) components of motion [e.g., *Wright et al.*, 2004; *Biggs et al.*, 2009b]. To achieve this, we identified interferogram pairs with different look directions (descending Envisat IM and ascending ALOS, Table 2) that cover a similar time period (overlapping to within 1 month) and hence identical deformation signal. We selected separate interferogram pairs for the uplift and subsidence periods and use these to evaluate whether analytical source models fit the deformation profiles (section 4.2).

It is important to recognize that as we only have two interferograms (from ascending and descending orbits) we cannot resolve the volcano's true 3-D deformation field. We assume that north-south motion was negligible and effectively resolve the deformation into a 2-D plane with axes running vertically and east-west [*Biggs et al.*, 2009b]. This assumption is valid because ascending and descending satellites look from close to due east and west, respectively, and will only capture a very minor component of north-south motion [*Ebmeier et al.*, 2010]. Further, when comparing analytical source models (outlined below) to the components of motion (section 4.2) we only compare east-west profiles through the deformation center, thus minimizing any north-south motion.

At present there are no additional constraints on the radius or shape of the deep reservoirs (e.g., from seismology or petrology) and so we only use simple analytical models (point source and penny-shaped crack geometries) [*Mogi*, 1958; *Fialko et al.*, 2001] to generate first-order constraints on the depth and geometry of the deformation sources. These models assume that crust is linearly elastic (i.e., they do not take into account crustal heterogeneities or the role of pore fluids), and in the case of the Mogi point source it is assumed that source depth is significantly larger than radius. Although these models are an oversimplification of the real earth they are an important first step toward understanding sources of volcanic deformation [*Segall*, 2010] and are appropriate when distinguishing between shallow- and deep-seated deformation mechanisms [e.g., *Mann and Freymueller*, 2003].
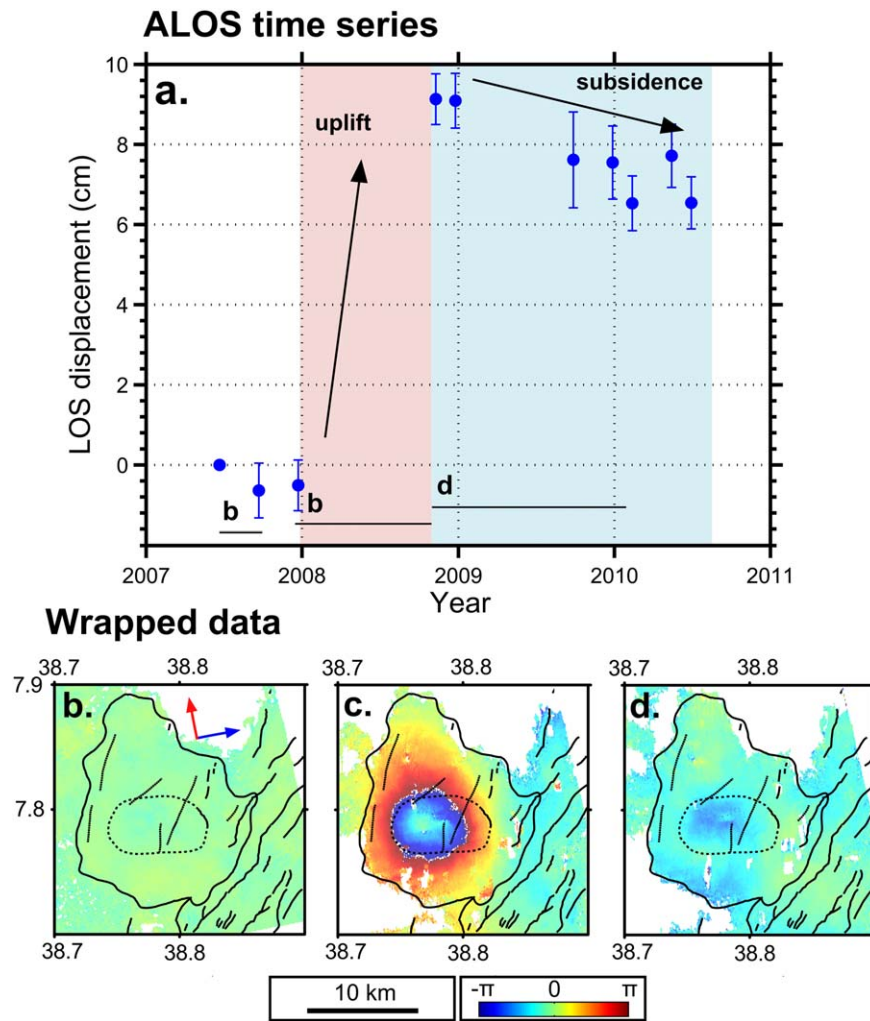
Figure 3. (a) ALOS line of sight (LOS) displacement time series. Note that the reference pixel location is identical to that shown in Figure 2a. (b)–(d) Example interferograms that correspond to the time period shown in the time series (labeled as black horizontal lines in Figure 3a). Each fringe represents 11.8 cm of LOS displacement (note that this is different from the Envisat data in Figures 2, 4, and 5). The black outline marks the extent of volcanic deposits, dashed line delineates the hypothesized ring fracture beneath Aluto [after *Hutchison et al.*, 2015], and NE-SW trending lines indicate tectonic faults [after *Agostini et al.*, 2011]. The red arrow indicates orientation of satellite orbit, and the blue arrow indicates the look direction of the satellite.

3.3. Joint Inversion of Geodetic Observations

Our study has focused on generating a dense coverage of observations between 2007 and 2011 as this covers an episode of uplift at Aluto [*Biggs et al.*, 2011] when both ALOS and Envisat satellites were operational and acquiring data (Table 1). If we assume a fixed source geometry then we can use a joint inversion technique [e.g., *Biggs et al.*, 2010; *Parks et al.*, 2015] to combine the InSAR data acquired from different satellites and tracks, to produce a time series of subsurface volume change. The advantage of this approach is that it allows us to combine independent deformation measurements (made at different times and from distinct viewing geometries) and thus greatly improve the temporal resolution of the data set [*Biggs et al.*, 2010].

Following *Biggs et al.* [2010], we make two main assumptions: (1) that all deformation is related to a single fixed source and (2) this source approximates a point pressure variation at depth within an elastic crust (i.e., a Mogi source, *Mogi* [1958] is used to convert our displacement time series to volume change). Previously, *Biggs et al.* [2011] used penny-shaped crack geometries [*Fialko et al.*, 2001] to model deformation at Aluto. However, as we shall show in section 4.2, penny models cannot reproduce the large horizontal components of deformation and in addition the shallow depth (<2 km) and large radius (5–10 km) required for these models are well beyond the known limits of the geothermal field (section 6). Mogi models provide a
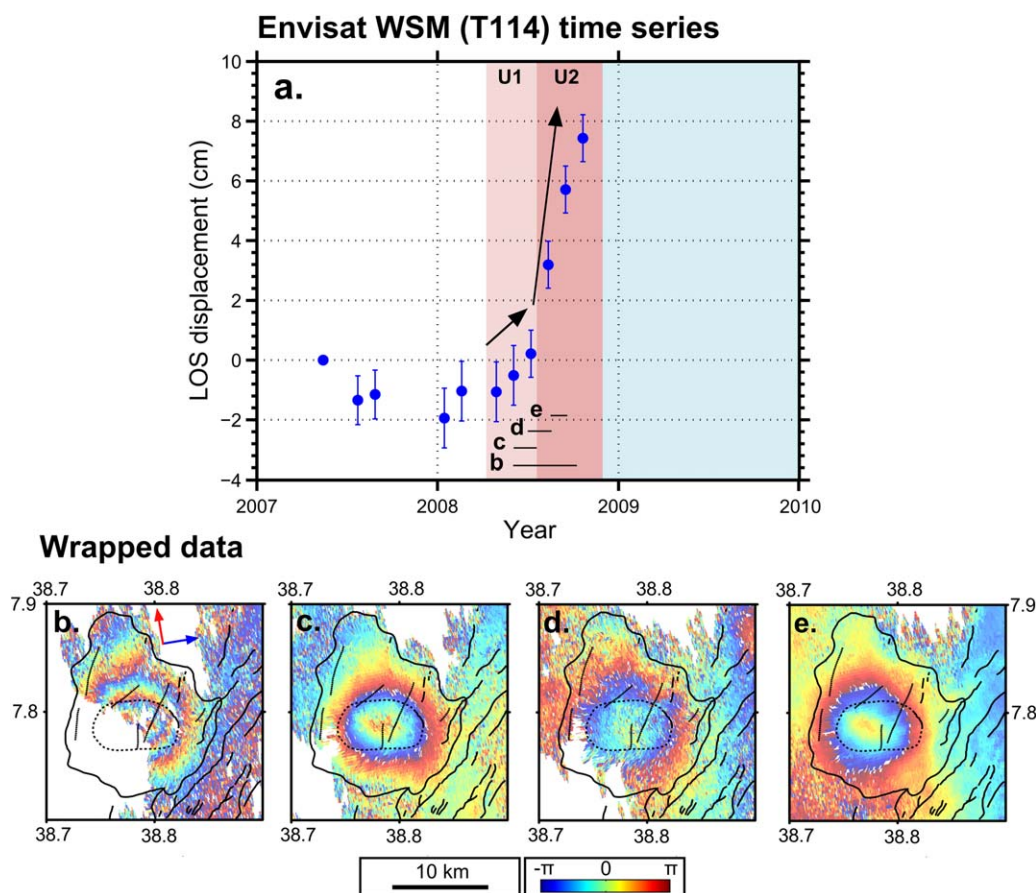
Figure 4. (a) Envisat WSM track 386 line of sight (LOS) displacement time series. Note that the reference pixel location is identical to that shown in Figure 2a. (b)–(e) Example interferograms that correspond to the time period shown in the time series (labeled as black horizontal lines in Figure 4a). Each fringe represents 2.83 cm of LOS displacement. The black outline marks the extent of volcanic deposits, dashed line delineates the hypothesized ring fracture beneath Aluto [after *Hutchison et al.*, 2015], and NE-SW trending lines indicate tectonic faults [after *Agostini et al.*, 2011]. The red arrow indicates orientation of satellite orbit, and the blue arrow indicates the look direction of the satellite.

significantly better fit to the components of motion (section 4.4) and so our assumption that all deformation between 2007 and 2011 relates to a Mogi source is reasonable.

To find the best-fitting source location and depth, we carried out a three-dimensional grid search by minimizing the misfit between the observations and the Mogi model. In the joint inversion, we assume that the source location is fixed through time and found our best-fitting sources converged at a depth interval of 4.8–5.4 km depth (section 4.3). In reality, the plumbing system of Aluto is likely to be significantly more complex than can be represented by a single Mogi source, and although our modeling in section 4.2 suggests that a slightly shallower Mogi source at ∼3.5 km provides a notionally better fit for the subsidence, for simplicity and because the majority of our data are from the uplift period, we model all volume change with a single ∼5 km deep source that can reproduce the bulk of the deformation across this unrest period.

We estimate the incremental volume change of the Mogi source, using equations (7) and (8) of *Biggs et al.* [2010] and then integrate these to provide a time series of volume change. We solved for several different sources of noise or nuisance parameters: those that were temporally and spatially correlated and those that were uncorrelated. More detailed information regarding both the inversion technique and error estimation may be found in *Biggs et al.* [2010].

3.4. Gas Chemistry and CO_2-$\delta^{13}C$ Analysis

Diffuse degassing through soil and low temperature fumarole vents (<100°C) is the main outlet for volcanic gases on Aluto [*Hutchison et al.*, 2015]. Between January 2012 and February 2014, we made ∼800 soil-gas CO_2 flux measurements to capture the large scale structural controls on degassing and resolve smaller scale
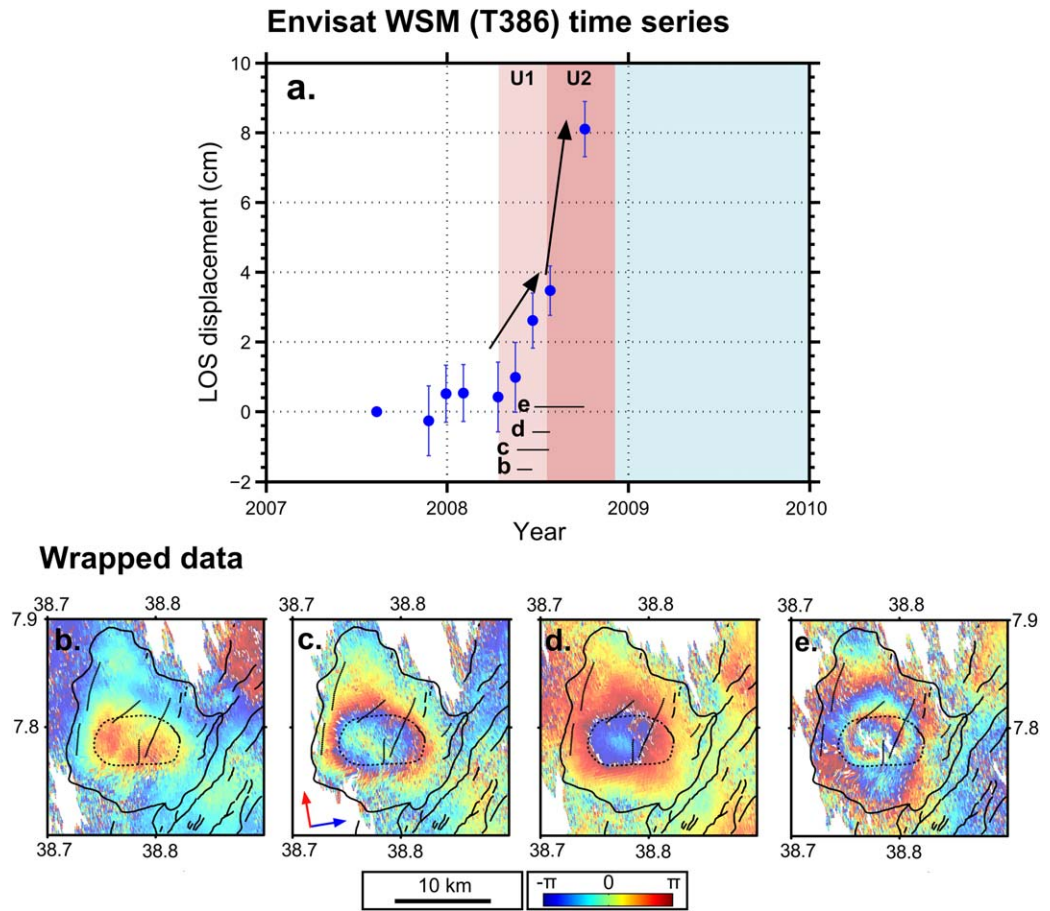
Figure 5. Envisat WSM track 114 line of sight (LOS) displacement time series. Note that the reference pixel location is identical to that shown in Figure 2a. (b)–(e) Example interferograms that correspond to the time period shown in the time series (labeled as black horizontal lines in Figure 5a). Each fringe represents 2.83 cm of LOS displacement. The black outline marks the extent of volcanic deposits, dashed line delineates the hypothesized ring fracture beneath Aluto [after *Hutchison et al.*, 2015], and NE-SW trending lines indicate tectonic faults [after *Agostini et al.*, 2011]. The red arrow indicates orientation of satellite orbit, and the blue arrow indicates the look direction of the satellite.

(30 m) variations along the AJFZ (Figure 2a) where 560 of these measurements were concentrated (detailed in *Hutchison et al.* [2015]). In February 2014, we also collected ~100 soil-gas samples from nine sites along AJFZ while conducting diffuse CO_2 degassing surveys. We adopted the method of *Chiodini et al.* [2008] to sample gas for laboratory analysis. At each measurement station, we set up an accumulation chamber [*Chiodini et al.*, 1998] and inserted a T-connector with a pierceable septum in the flowline just after the infrared gas analyser. During the CO_2 flux measurements, we pierced the septum with a syringe and extracted 10 ml of gas. The syringe had a built-in shut off valve and so the sample gas was sealed, and then subsequently injected into an evacuated vial through a pierceable butyl rubber septum. Two gas samples were extracted during each measurement. The first was taken after a few seconds allowing homogenization of gases within the chamber; the second sample was collected 40 s later, at higher CO_2 concentration. The first sample (0 s) allows local anthropogenic air pollution effects to be characterized [e.g., *Chiodini et al.*, 2008] (this was minimal at Aluto), and more importantly, it can be used to distinguish contributions from other sources (e.g., biogenic) before volcanic gases inundate the chamber.

Bulk gas compositions were measured for seven samples (Table 3) at the Department of Earth and Planetary Sciences at University of New Mexico (UNM). A combination of gas chromatography (GC) and quadrupole mass spectrometry (QMS) were used to measure the composition of gases. CH_4, CO_2, H_2, and CO concentrations were measured using GC, while Ar, He, N_2, and O_2 were determined using QMS. An analytical uncertainty of <0.1% was reported for gas analyses by the QMS system at UNM by *de Moor et al.* [2013a]. Further, *Lee et al.* [2016] used the same GC and QMS system for bulk gas analyses of vials collected from an accumulation chamber and estimated the analytical uncertainty of the GC measurements to be ±2% based on

repeat measurements. It is important to recognize that the pierceable glass vials are not designed for storage of H_2 and He gas species and although these were analyzed at UNM we believe that these species were likely to have been lost either by diffusion through glass or through the rubber septum. Therefore, the values presented for H_2 and He are minima.

Carbon isotope measurements of CO_2 (CO_2-$\delta^{13}C$) were made for the majority of samples at the Geochemistry Laboratory of INGV-Osservatorio Vesuviano (Naples). Gases were analyzed within a few days of sampling, thus minimizing CO_2 gas loss and isotopic fractionation through the septum [*Tu et al.*, 2001]. The samples were analyzed using a continuous flow isotope ratio mass spectrometer (Thermo-Finnigan Delta XP) interfaced with a Gasbench II device equipped with autosampler. CO_2-$\delta^{13}C$ measurements were also made for seven samples at the Center for Stable Isotopes, UNM (the same samples that were also analyzed for bulk gas chemistry, Table 3). At UNM CO_2-$\delta^{13}C$ were measured by Isotope Ratio Mass Spectrometer (Finnigan Delta XL) with a gas bench and auto-sampler. Results for all CO_2-$\delta^{13}C$ measurements are shown in delta notation as per mil values ($\delta‰$) relative to Pee Dee belemnite (PDB) using an internal standard and are characterized by a $\delta^{13}C$ standard error of $\pm 0.1‰$ (supporting information Table S1).

It was not possible to make a direct comparison of an identical soil-gas sample measured for CO_2-$\delta^{13}C$ between the different laboratories at UNM and Naples. However, at site 06A (supporting information Table S1) where the natural CO_2-$\delta^{13}C$ variation was well constrained by samples analyzed in Naples (i.e., all nine gas samples were between $-4.2‰$ and $-4.5‰$) we found that the corresponding measurements made at UNM were $-4.2‰$ and $-4.3‰$ (Table 3). The overlapping values suggest that any systematic error in isotopic measurements between the different laboratories were within the natural variability of the soil-gas sampling sites on Aluto (section 5).

4. Ground Deformation at Aluto

4.1. Displacement Time Series and Spatial Patterns

Interferograms and displacement time series for each track are shown in Figures 2–5. Note that as surface displacements are measured in the satellite LOS, the difference in the apparent location of the center of uplift and the magnitude of the signal in interferograms (Figures 2–5) primarily results from differences in the satellite azimuths and incidence angles of the radar pulse (Table 1). In Figure 2a, the main structural features on and around the Aluto volcanic complex are shown, they include NNE-SSW-trending Wonji faults, an elliptical caldera rim and ring fault that is hypothesized to underlie the Aluto complex [*Hutchison et al.*, 2015]. The extent of volcanic deposits from the complex is also highlighted by the irregular dotted outline.

The Envisat IM data provide the longest displacement time series and suggest there have been two major uplift events at Aluto between 2004 and 2011 of magnitude $+15$ cm (2004) and $+10$ cm (2008); in both cases, these were followed by a period of slow subsidence (~ -5 cm) which took place over several years (Figure 2b) [*Biggs et al.*, 2011]. The available ALOS and Envisat WSM data (Table 1) are concentrated on the second period of uplift at Aluto between 2008 and 2009 and show maximum LOS displacement between $+8$ and $+10$ cm (Figures 3a, 4a, and 5a), consistent in magnitude with the Envisat IM observations (Figure 2b). The new ALOS data also support the period of slow subsidence after 2009 (Figure 3a), consistent with Envisat IM observations (Figure 2a) and further evidence that the long-term deformation pattern of Aluto is characterized by short uplift events (<1 year) followed by more gradual subsidence (over several years). Envisat WSM data provide the highest temporal resolution snapshot and suggest that there are two phases to the uplift pulse (marked U1 and U2, in Figures 4a and 5a). The initial phase (U1) has a displacement of $+2-3$ cm over a 3 month period between April and July 2008, the rate then increases between July and October (U2) where $+5$ cm of deformation occurs over 3 months. We suggest that the WSM interferograms indicate a two-step accelerating deformation trend.

The Envisat IM and WSM interferograms all show an elliptical deformation signal with east-west to ESE-WNW elongation. The center of the deformation (for both uplift-subsidence events, Figure 2) is remarkably consistent throughout the observation period and, based on the Envisat look direction, is located a few kilometers east of the caldera center. The deformation signals for the ALOS data appear more circular (Figure 3c) and the subsidence pattern shows only slight elongation east-west (Figure 3d). Comparing the deformation signals on Aluto to the major volcanic and tectonic features, we note several important features. First, all uplift signals extend beyond the main edifice and proposed ring fault of *Hutchison et al.* [2015] but are

Table 2. Summary of Satellite Data Used to Elucidate Components of Motion, and the Analytical Source Models Used to Fit the Profile Lines in Figure 6

	Data			Models			
					Parameters		
	Satellite	Date 1	Date 2	Source type	Depth (m)	Radius (m)	Misfit (cm)
Uplift	ALOS	23 Dec 2007	09 Nov 2008	Mogi	5100		1.12
	Envisat IM	26 Dec 2007	05 Nov 2008	Penny	2500	6300	2.29
Subsidence	ALOS	09 Nov 2008	15 May 2010	Mogi	5100		0.65
	Envisat IM	05 Nov 2008	14 Apr 2010	Mogi	3400		0.54
				Penny	1800	4400	0.83

Note: Misfit for this study is the rms error between the model and data (Ux and Uz components) along the profile lines.

contained within the area covered by volcanic deposits. Moreover, all uplift and subsidence signals show no clear alignment or termination of the deformation along the major tectonic structures (N.B. very minor discontinuities in phase are identified across some fault structures, e.g., Figure 2d, 2f, Figure 5d, these are
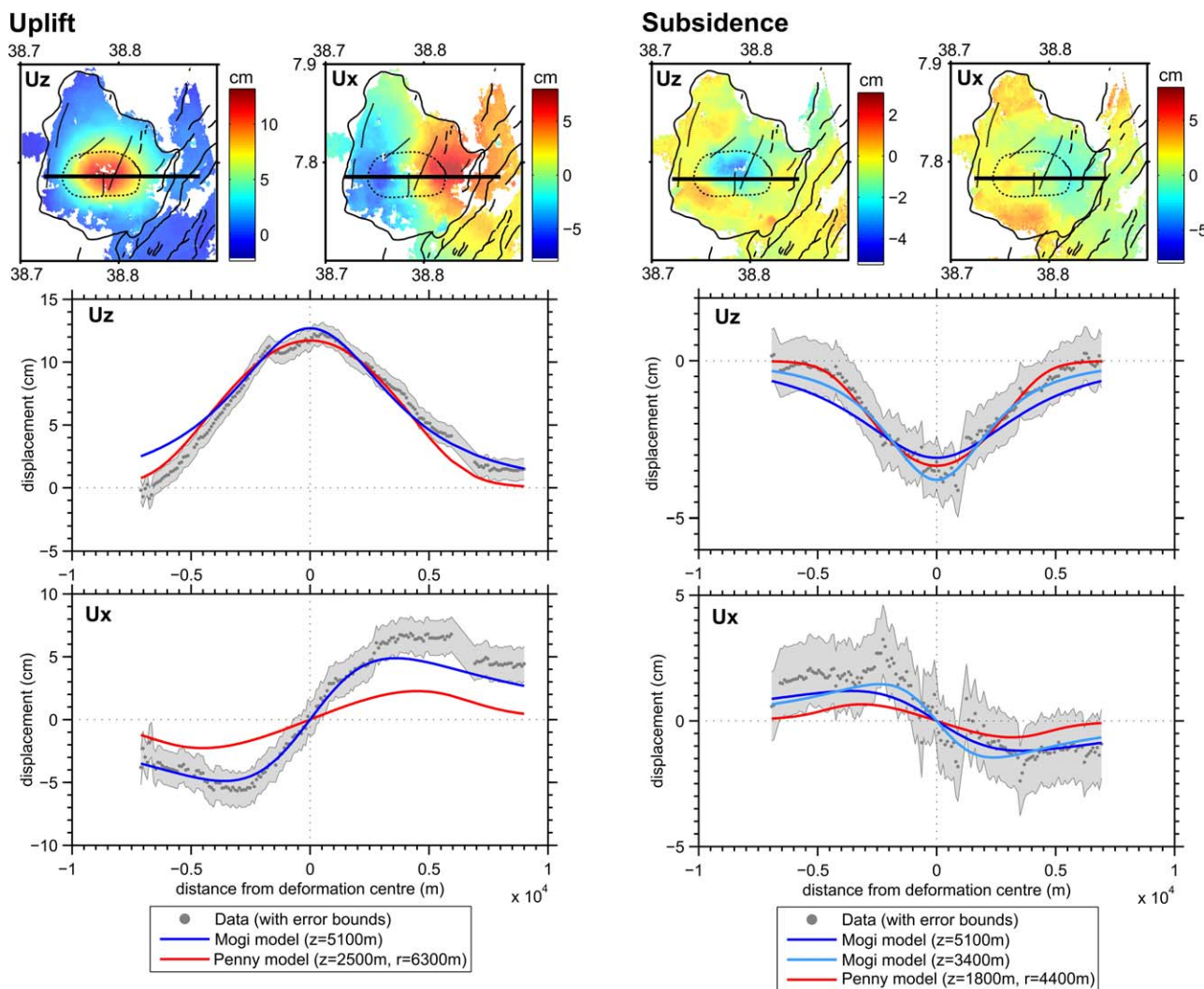

Figure 6. Comparison of the vertical (Uz) and horizontal (Ux) components of motion derived from InSAR data with deformation fields predicted by a variety of source models. The uplift and subsidence deformation phases are shown separately. InSAR displacement measurements are from the east-west profiles marked by the black line on the displacement maps at the top of the figure. The black outline marks the extent of volcanic deposits, dashed line delineates the hypothesized ring fracture beneath Aluto [after *Hutchison et al.*, 2015], and NE-SW trending lines indicate tectonic faults [after *Agostini et al.*, 2011].

Table 3. Composition of Soil-Gas Efflux From the Artu Jawe Fault Zone Sampled in February 2014 and Subsequently Measured at the University of New Mexico (UNM)

Sample ID	Ar (%)	N$_2$ (%)	O$_2$ (%)	CO$_2$ (%)	CO$_2$-δ^{13}C (‰)	H$_2$ (ppm)	He (ppm)	CH$_4$ (ppm)	CO (ppm)	N$_2$/O$_2$	N$_2$/Ar	CO$_2$/N$_2$
01-A3 40s	0.76	78.75	18.17	2.31	−4.41	6.11	23.10	25.53	33.62	4.3	103	0.03
01-B1 40s	0.86	76.21	20.72	2.20	−3.54	9.82	28.72	b.d.	37.26	3.7	89	0.03
01-B4 40s	0.72	80.05	17.43	1.79	−4.26	8.33	32.74	b.d.	47.25	4.6	110	0.02
01-B7 40s	0.87	76.67	21.01	1.45	−6.08	7.75	46.63	b.d.	45.15	3.6	88	0.02
01-C1 40s	0.87	77.05	20.84	1.23	−3.89	9.34	19.27	b.d.	35.34	3.7	88	0.02
03-A3 40s	0.90	77.27	21.02	0.81	−5.93	9.06	24.86	b.d.	35.00	3.7	86	0.01
06-A1 40s	0.73	72.19	16.93	10.03	−4.26	9.60	18.36	1053.00	64.44	4.3	99	0.14
06-A4 40s	0.80	69.89	19.12	10.12	−4.22	10.02	21.86	621.51	35.70	3.7	88	0.14

Note: Gas sampling sites are shown in Figure 10 and are linked to the Sample ID. CH$_4$, CO$_2$, H$_2$, and CO concentrations were measured using gas chromatography (GC) techniques. Ar, He, N$_2$, and O$_2$ were measured via quadrupole mass spectrometry (QMS). Analytical uncertainty for the GC measurements is at ±5%, and QMS analyses at <0.1% (concentration), see section 3.3. CO$_2$-δ^{13}C measurements were also made by Isotope Ratio Mass Spectrometer for seven samples at the Center for Stable Isotopes, UNM. Results for CO$_2$-δ^{13}C are shown in delta notation as per mil values (δ‰) relative to PDB (Pee Dee belemnite) and are characterized by a δ^{13}C standard error of ±0.1‰. Note that H$_2$ and He concentrations represent minima. b.d.: below detection limit.

likely coincidental and our overwhelming observation is that deformation fringes show no significant change across the mapped faults). Fault structures do not influence the deformation patterns; they simply act as pathways for fluid release (developed further in section 5).

4.2. Components of Motion and Deformation Source Models

Previously, *Biggs et al.* [2011] used Envisat IM data (section 4.1) to evaluate best fitting point source [*Mogi*, 1958] and penny-shaped crack [*Fialko et al.*, 2001] geometries for Aluto. While their best-fitting model was a shallow (<2.5 km) penny-shaped crack with large radius (3–10 km), it is important to recognize that a point source at greater depths can produce a similar ground deformation to a penny-shaped crack [*Fialko et al.*, 2001].

Here we exploit the different look directions of the interferograms (i.e., Envisat and ALOS) to decompose the LOS motion into horizontal and vertical components (section 3.2). The vertical (Uz) and horizontal (Ux) components of deformation are shown in Figure 6 for both the uplift and subsidence phases of deformation. East-west profile lines taken through the center of the deformation pulse (and hence minimizing the north-south component of motion, section 3.2) are also shown in Figure 6. Profiles reveal that the 2008 uplift Uz$_{max}$ is 12 ± 1 cm and Ux$_{max}$ is 6 ± 2 cm, while for the subsidence between end-2008 and mid-2010 Uz$_{min}$ is 3.5 ± 1.5 cm while Ux$_{max}$ is 2 ± 2 cm. Note that for both the uplift and subsidence, the ratio of maximum horizontal to maximum vertical displacement is ∼0.5, much greater than a penny geometry which is normally less than 0.3, and closer to a spherical (Mogi) source which is about 0.4 [*Fialko et al.*, 2001; *Yun et al.*, 2006].

To further distinguish between the two end members models (i.e., the shallow penny-shaped crack and the deeper Mogi point source), we carry out a nonlinear inversion procedure to find the optimum model parameters that match the components of motion observed along the profile lines (Figure 6). To evaluate the quality of each fit, we calculate the root mean square error (RMSE) between the model and data along the profile line (shown in Table 2).

Mogi models (Figure 6) at a depth of ∼5 km provide a reasonable fit to both the Ux and Uz components for the uplift and subsidence (with misfit of 1.12 and 0.65 cm, respectively, Table 2). When we attempted to minimize the misfit for both the Ux and Uz components for the penny model the inversion procedure did not provide a unique solution. In other words, the large ratio of horizontal to vertical components that we observe in both the uplift and subsidence phases could not be reproduced by a penny source model. Instead we have only inverted the penny model for the Uz component of our data (Figure 6). While the penny model can reproduce the Uz component, it is evident that it greatly underestimates the Ux components (misfits of 2.29 and 0.83 cm, for uplift and subsidence respectively, Table 2). On this basis, we consider it unlikely that a shallow penny source is the main driver for deformation events on Aluto.

Although our analysis of deformation components primarily seeks to discriminate between shallow (penny) and deep (Mogi) model geometries, it is interesting to note that a Mogi model at 3.4 km provides a better fit for the subsidence than a source at 5.1 km as was identified for the uplift phase (misfits are 0.54 and 0.65 cm, respectively, Table 2). Our InSAR dataset has limited temporal coverage of the subsidence phase
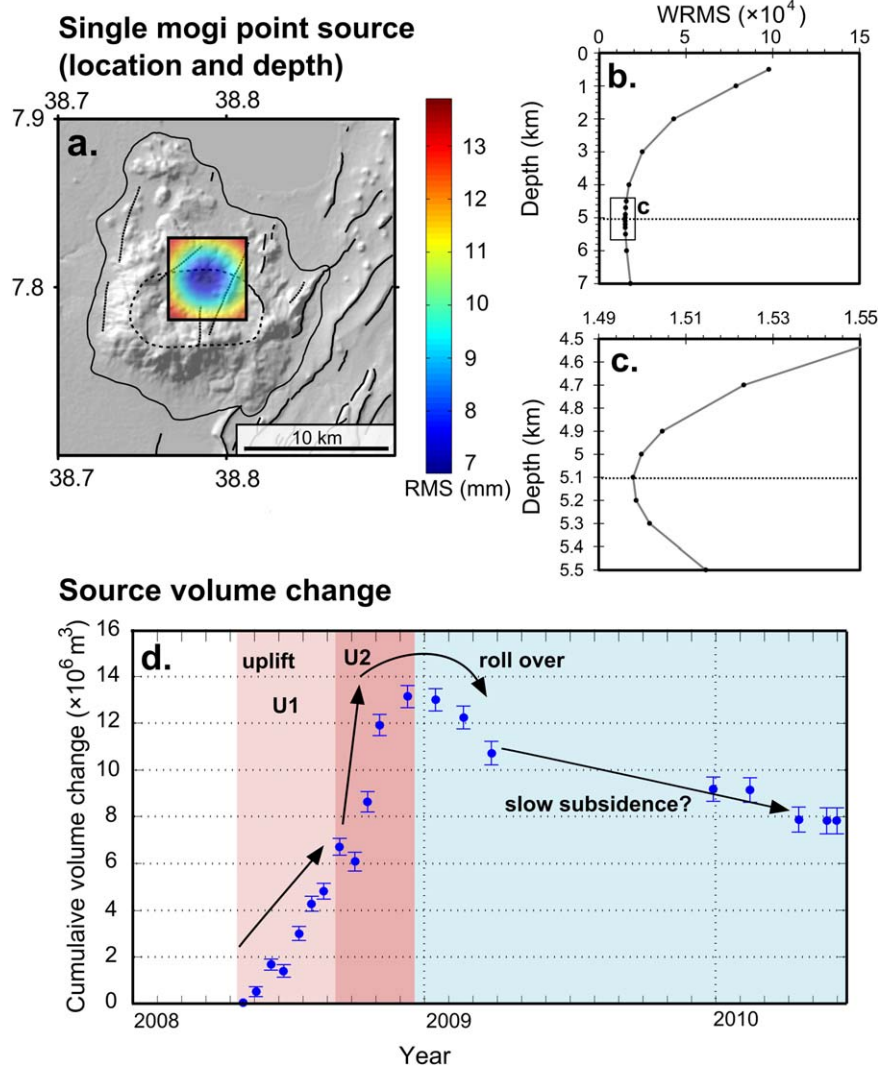
Figure 7. Joint inversion models of InSAR data and cumulative volume time series. (a) Grid search to find minimum RMS misfit (blue) and best source location. The black outline marks the extent of volcanic deposits, dashed line delineates the hypothesized ring fracture beneath Aluto [after *Hutchison et al.*, 2015], and NE-SW trending lines indicate tectonic faults [after *Agostini et al.*, 2011]. (b) and (c) Source depth versus minimum weighted residual for each inversion (WRMS). The best fit depth is found to be at 5.1 km (Figure 7c is a zoomed in view of the area of the plot shown in Figure 7b indicated by the vertical rectangle). (d) Cumulative variation in volume change derived from the joint inversion of InSAR measurements covering the 2008–2010 period.

(Figures 2 and 3) and does not allow us to thoroughly investigate whether or not the deformation source remains stable during the deflation period (e.g., evolving to shallower depths with time). A more complete understanding of the temporal evolution of the deformation sources at Aluto will be revealed by recently deployed continuous GPS networks and new radar satellites (e.g., Sentinel-1) that have significantly improved repeat times.

4.3. Joint Inversion of Deformation Data

We used the interferograms covering the uplift-subsidence period between 2008 and 2010 to estimate the volume changes that could explain the observed deformation trend (Figure 7). The best fitting spherical source location and optimum depth was found by carrying out a grid search (Figure 7a) and finding the minimum weighted residual for each inversion (Figures 7b and 7c). The best source is shown to be at a depth of 5.1 km broadly consistent with the models in Figure 6. The total volume increase for the uplift period is $+13 \pm 0.5 \times 10^6$ m^3, followed by $-5 \pm 1 \times 10^6$ m^3 of volume decrease between the end of 2009 and 2010 (subsidence period).
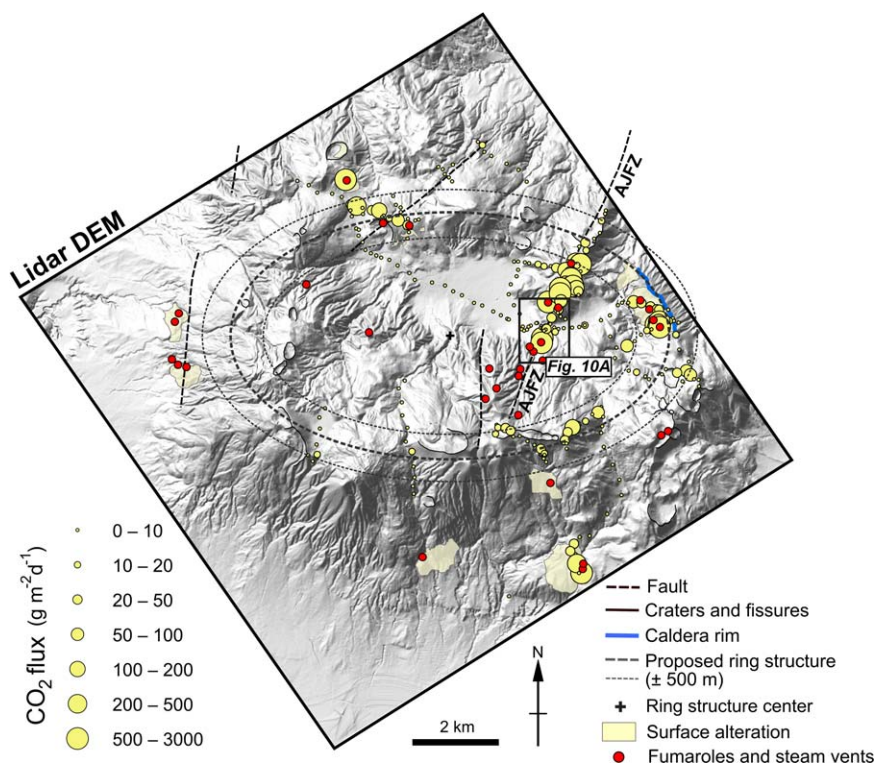
Figure 8. Lidar hillshade DEM covering the main edifice of Aluto volcano overlain with CO_2 degassing observations and structural interpretations [after *Hutchison et al.*, 2015]. All soil-CO_2 flux measurements shown in this figure were made in January to February and November 2012. The magnitude of the soil-CO_2 flux corresponds to the size of the circle in accordance with the key on the lower left of the plot. Faults on the complex have been described by *Hutchison et al.* [2015] and were mapped using remote sensing imagery or were suggested by previous geological reports and deep well data [*Kebede et al.*, 1985; *ELC Electroconsult*, 1986; *Gizaw*, 1993; *Gianelli and Teklemariam*, 1993]. The dashed ellipses show the size and orientation of a buried ring fault that may explain anomalous degassing zones around the rim of the edifice (see *Hutchison et al.* [2015] for detailed explanation). The fine dashed ellipses represent ±500 m uncertainty bounds on the central ellipse. The mapped caldera rim is shown in blue and overlaps the proposed ring structure. Fumaroles vents and zones of surface alteration were mapped using a combination of field and remote sensing observations [*Kebede et al.*, 1985; *Hutchison et al.*, 2015]. The black box inset links to Figure 10a, where a dense grid of soil-CO_2 flux measurements was undertaken and all gas samples (section 5) were collected.

Combining the individual interferograms from the different tracks demonstrates that the rate of volume change accelerated through 2008 (shown as the step between U1 and U2 in Figure 7d). This is consistent with the two-step uplift pattern which we identified in the LOS displacement time series from WSM data (Figures 4a and 5a). At the point of maximum source volume change between November 2008 and January 2009, the time series (Figure 7d) shows a distinct "roll over" into negative volume change (i.e., deflation). Finally, although there is a considerable gap in measurements during the presumed slow subsidence (deflation) period through most of 2009 and early-2010, the volume time series (Figure 7d) indicates that a significant component of the deflation ($\sim$50%, equivalent to $\sim-2 \times 10^6$ m^3) took place in the 3 months immediately following peak uplift.

5. Volcanic Degassing at Aluto

5.1. Degassing Patterns and Compositional Overview

The large scale pattern of gas emissions on Aluto is shown in Figure 8 where CO_2 flux measurements, made in January to February and November 2012, are overlain on a lidar DEM. As discussed by *Hutchison et al.* [2015], fumarole vents, hydrothermal alteration, and sites of anomalously high CO_2 gas fluxes (i.e., $>$10 g m^{-2} d^{-1}) on Aluto are often associated with major structural features. The NNE-SSW trending AJFZ (Figure 8) is a clear example of a tectonic lineament and elevated CO_2 flux values can be traced for $>$3 km along the length of the fault zone. An elliptical ring fracture structure (outlined by *Hutchison et al.* [2015]) can explain fumaroles and steam vents immediately west of the caldera rim (Figure 8) and could also account for anomalous diffuse degassing regions identified on the southern and north-eastern rims of the edifice.
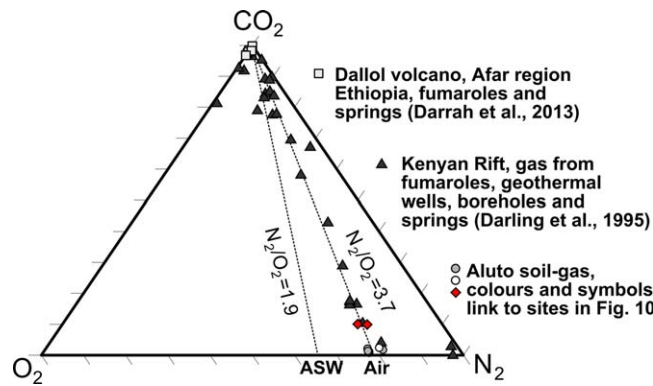
Figure 9. CO_2-O_2-N_2 triangular plot for soil-gas samples collected in this study (see Table 3) at Aluto volcano (circles and diamonds), as well as gas phase samples collected at Dallol volcano, Afar, Ethiopia (squares) [*Darrah et al.*, 2013] and throughout the Kenyan Rift (triangles) [*Darling et al.*, 1995]. The Aluto samples fall on a mixing line between air and pure-CO_2 end member, although are evidently dominated by air.

The chemical composition of the dry (water-free) gas-phase in the soil-gas samples collected from the AJFZ in February 2014 are reported in Table 3, and summarized in the CO_2-O_2-N_2 triangular diagram in Figure 9. The gas sampling sites are also shown as colored symbols in Figure 10a where they are overlain on aerial imagery and gridded soil-CO_2 flux (measured at the time) [*Hutchison et al.*, 2015].

The soil gas samples are dominated by N_2 (69–80%) and O_2 (16–21%) and represent air contaminated by a volcanic component rich in CO_2 (1–10%, Table 3). This is corroborated by the triangular diagram in Figure 9 which shows that the Aluto soil-gas samples fall on a mixing line between air and a pure-CO_2 end member. CH_4 was above detection only in the samples with the highest CO_2 concentrations (Table 3) while CO was between 33 and 65 ppm. CH_4 (when above detection limits) was significantly greater than atmospheric
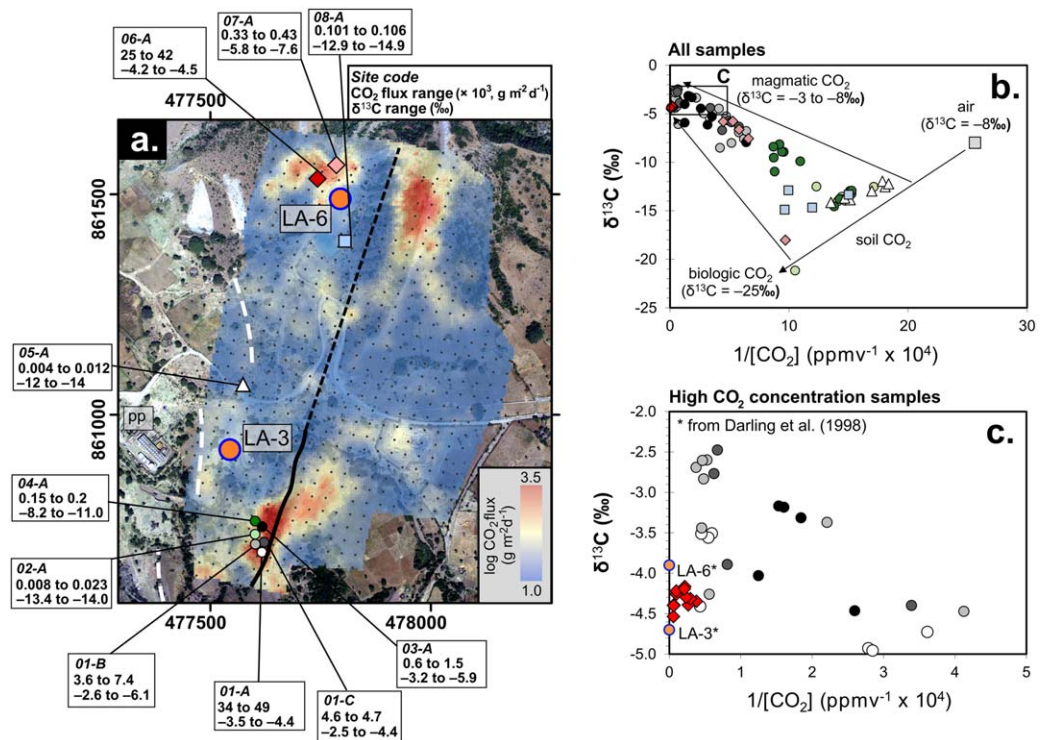

Figure 10. Degassing sites along the Artu Jawe fault zone (AJFZ). (a) Gas sampling sites along the fault zone are shown as colored symbols. Orange circles with blue outlines identify the location of the productive geothermal wells (LA-3 and LA-6). The sampling locations are overlain on an aerial photo and a CO_2-flux map (blue to red colors, described by *Hutchison et al.* [2015]). Small gray points represent a discrete CO_2 flux measurement. The black line indicates the Artu Jawe fault scarp (black) and its projected continuation north (dashed). Less-pronounced breaks in topography (10–20 m high) west of the main fault scarp are marked by white dashed lines. pp: the Aluto-Langano geothermal power plant. The range of soil CO_2 flux and CO_2-$\delta^{13}C$ (for the 40 second samples, section 3.3) for each site are shown in the white boxes around the grid. (b) Carbon isotopic composition ($\delta^{13}C$) of soil CO_2 efflux plotted against the reciprocal of CO_2 concentration in the gas samples (symbols are linked to map view in Figure 10a). This plot shows all samples that were collected and analyzed for CO_2-$\delta^{13}C$ (both the 0 and 40 s samples, section 3.3). The data define a triangular array that can be defined by mixing between between air, an end-member characterized by high CO_2 concentrations and light $\delta^{13}C$ values approaching $-25‰$ (i.e., biogenic CO_2) and an end-member characterized by high CO_2 concentrations and heavier $\delta^{13}C$ values (i.e., magmatic CO_2). (c) Inset of Figure 10b showing CO_2-$\delta^{13}C$ for the highest concentration samples. CO_2-$\delta^{13}C$ of gases from geothermal wells on Aluto are shown after *Darling* [1998]. Note that deep well samples contain ~98% CO_2 (dry gas phase). The full CO_2-$\delta^{13}C$ data set is provided in the supporting information file.

concentrations and it is likely that this species is produced by reducing reactions in the hydrothermal reservoir [e.g., *Agusto et al.*, 2013; *Tassi et al.*, 2013].

In Figure 9, we also show gas-phase analyses made at fumaroles, geothermal wells, springs, and boreholes, at active geothermal areas along the Kenyan Rift [after *Darling et al.*, 1995] and at Dallol volcano located in Afar, Ethiopia [after *Darrah et al.*, 2013]. Although high temperature magmatic gas analyses have been analyzed at the basaltic Erta Ale volcano [*de Moor et al.*, 2013b], there are very few low temperature gas-phase analyses available for other geothermal sites in Ethiopia that we could directly compare to Aluto. The regional comparison shown in Figure 9 does, however, illustrate that geothermal gases sampled from across the EARS can be broadly defined by mixing between air, air saturated water, and a CO_2-rich end-member that is of magmatic/mantle origin [e.g., *Darling et al.*, 1995; *Barry et al.*, 2013; *Darrah et al.*, 2013; *de Moor et al.*, 2013a].

CO_2-$\delta^{13}C$ data from the AJFZ of Aluto are presented in Figure 10b (symbols are linked to the CO_2-flux map in Figure 10a). The values span a range between $-21.2‰$ and $-2.5‰$, and define a triangular array when plotted as the reciprocal of CO_2 concentration (Figure 10b) [after *Chiodini et al.*, 2008; *Parks et al.*, 2013]. Overall the CO_2-$\delta^{13}C$ array (Figure 10b) can be defined by three end-member components: magmatic $\delta^{13}C$ values (between $-3‰$ and $-8‰$) [*Gerlach and Taylor*, 1990; *Javoy and Pineau*, 1991; *Macpherson and Mattey*, 1994; *Sano and Marty*, 1995]; atmospheric $\delta^{13}C$ values ($-8‰$) [*Darling et al.*, 1995; *Tedesco et al.*, 2010] and biogenic $\delta^{13}C$ values ($-20‰$ to $-25‰$) [*Cheng*, 1996; *Chiodini et al.*, 2008].

The samples with highest CO_2 concentrations (sample site 06-A, Figure 10a and Table 3) show a narrow range of CO_2-$\delta^{13}C$ values from $-4.2‰$ to $-4.5‰$, strongly supporting a magmatic origin (Figure 10c). The key inference that the CO_2-$\delta^{13}C$ data allows us to make is that the magmatic and geothermal reservoirs of Aluto are physically connected. Volatiles released by the magma reservoir degas into a deep geothermal reservoir at >2 km (section 6) [*Gizaw*, 1993; *Teklemariam et al.*, 1996]. While the exact interactions of the magmatic CO_2 gas with the fluids in the geothermal reservoir are likely to vary (i.e., it may remain as a free gas, dissolve in the fluid and/or precipitate out through mineralization processes) [*Chiodini et al.*, 2015b], ultimately the CO_2-$\delta^{13}C$ of the gas and boiling fluid efflux that ascends along the AJFZ fingerprints this deep magmatic origin. There are several subtle features to note regarding the CO_2-$\delta^{13}C$ data set and these are explored in the following sections.

5.2. Spatial Variations in CO_2-$\delta^{13}C$

There are clear spatial variations in CO_2-$\delta^{13}C$ at different sample sites along the fault zone (Figure 10c). For example, fumarole vents at sites 06-A and 07-A at the northern end of the grid show distinct isotopic differences from fumaroles at sites 01-A, B, and C at the southern end; the latter show values that are up to $\sim$2‰ heavier (Figures 10a and 10c). While variations in gas flux along the AJFZ have previously been linked to the presence of deep structures and changes in near-surface permeability [*Hutchison et al.*, 2015], the distinct CO_2-$\delta^{13}C$ at different sites also suggests that there is limited mixing and homogenization of the gases along the fault zone.

5.3. Temporal Variations in Gas Flux and CO_2-$\delta^{13}C$

Short-timescale variations are also seen in soil-gas flux and CO_2-$\delta^{13}C$ at the measurement sites. For example, sites 01-A, B, and C were measured over the course of 1 h and were only separated by a few tens of meters. These sites show clear differences in both the absolute magnitude of soil-gas flux ($\sim$45, $\sim$7, and $\sim$5 $\times$ 10^3 g m^{-2} d^{-1}, respectively) and also the flux variation between measurements (30%, 50%, and 5%, respectively, Figure 8a). There is no correlation between soil-gas flux and CO_2-$\delta^{13}C$ at these three measurements sites: site 01-C, for example, shows a near constant soil-gas flux but $\sim$2‰ range in CO_2-$\delta^{13}C$ (Figure 10a). These observations clearly reveal that gas emissions at the surface of the fault zone are not stable through time, and that both gas flux and composition can vary over the course of a few minutes.

5.4. High CO_2-$\delta^{13}C$ Values

High CO_2 concentration samples (Figure 10c) collected from sites 01-B and C show a cluster of CO_2-$\delta^{13}C$ values between $-2.5‰$ and $-3.0‰$, above the range normally associated with magmatic gases ($-3‰$ to $-8‰$). There are a number of explanations as to why these values are slightly heavier than typical magmatic values:

I. Calcite precipitation: Loss of CO_2 due to calcite precipitation has the potential to fractionate CO_2-δ^{13}C. This process is temperature-dependent, such that at temperatures <192°C, calcite is enriched in ^{13}C relative to residual dissolved CO_2 in geothermal fluids, whereas at higher temperatures >192°C calcite becomes depleted in ^{13}C relative to residual CO_2 [*Bottinga*, 1969]. To explain the observations on Aluto would require high-temperature (>192°C) precipitation of calcite.

II. Phase partitioning and hydrothermal degassing: Vapor partitioning can be caused by either boiling (>100°C) and/or hydrothermal degassing due to supersaturation of a particular gas species. The loss of CO_2 from geothermal fluids via these processes will cause isotopic fractionation of CO_2-δ^{13}C [e.g., *Vogel et al.*, 1970; *Mook et al.*, 1974]. These processes are temperature dependent and at temperatures <110°C dissolved carbon species will be enriched in ^{13}C, leaving ^{13}C relatively depleted in the residual gas phases [*Szaran*, 1997]. At higher temperatures (>110°C), the isotopic fractionation is in the opposite sense and residual gases will consequently be enriched in ^{13}C. This latter case would again have to be true to explain the observed values of $\sim$−2.5‰ at Aluto (Figure 10c).

III. Crustal contamination: CO_2 gas could be released by decarbonation of limestone in the subvolcanic system, induced either by heating, or reaction with magma. These gases would yield a CO_2-δ^{13}C of +2–6‰ [*Lollar et al.*, 1997; *Tassi et al.*, 2010; *Darrah et al.*, 2013; *Parks et al.*, 2013], and when mixed with magmatic gases could explain the values of −2.5‰ observed.

To thoroughly investigate these processes further would require δ^{13}C analyses of the geothermal fluids, and also additional tracers, such as He [cf. *Barry et al.*, 2013, 2014]. However, until this data are available we can make several arguments. First, deep well data from LA-3 and LA-6 (Figure 10a) confirm that temperatures exceed 300°C beneath the surface of the AJFZ and that boiling takes place from at least 2100 m up to 700 m depth [*Gizaw*, 1993]. Calcite is also one of the main hydrothermal mineral precipitates at Aluto and has been identified in deep wells cores collected along this fault zone [*Teklemariam et al.*, 1996]. These constraints are consistent with both scenarios (i) and (ii), and favor carbon isotope fractionation by high-temperature calcite precipitation, boiling, and degassing within the geothermal system.

We can investigate the plausibility of crustal contamination (scenario iii) using a simple mass balance calculation. Assuming that the heavy CO_2-δ^{13}C values are entirely the result of crustal contamination, taking the magmatic end-member as −4.25‰ and assuming a carbonate contaminant of +4‰ (an average of the typical range noted above), it would require 30% carbonate to 70% magmatic input to explain the heaviest gases ($\sim$−2.5‰, Figure 10c). There is, however, no physical evidence from the petrography or geochemistry [*Di Paola*, 1972; *Weaver et al.*, 1972] of the Aluto rock samples to suggest that carbonate materials are incorporated into the melt. In addition, lacustrine sediment layers in the subsurface are thin (50–100 m, Figure 11) and do not contain significant carbonate horizons [*Gianelli and Teklemariam*, 1993; *Teklemariam et al.*, 1996]. Decarbonation might link to Jurassic-Palaeogene sedimentary rocks that make up basement lithologies in the MER [e.g., *Cornwell et al.*, 2010], however, their thickness and composition beneath Aluto are completely unknown.

Our preferred explanation is that geothermal processes (scenarios i and ii) cause some CO_2-δ^{13}C samples to be slightly heavier than the magmatic range; these scenarios can explain the elevated values without invoking contamination by unknown carbonate material. The AJFZ provides an important pathway for fluid upflow and migration from the geothermal reservoir to the surface (section 6). It is likely that upflow rates, as well as boiling, degassing, and mineral precipitation vary along the fault zone, and that these produce the complex spatial (section 5.2) and short-timescale (section 5.3) variations in both gas flux and CO_2-δ^{13}C.

6. Constraints on the Magmatic-Hydrothermal System

We now use constraints on the subsurface structure and geothermal field of Aluto to develop a conceptual model of the magmatic and hydrothermal systems (Figure 11). The original interpretations of Aluto's magmatic-hydrothermal system were largely based on deep well logs, cores and cuttings [e.g., *Gizaw*, 1993; *Gianelli and Teklemariam*, 1993; *Teklemariam et al.*, 1996]. In 2012, magnetotelluric surveys were carried out by *Samrock et al.* [2015] and their new resistivity model for Aluto has helped clarify many of the previous interpretations (outlined in detail below). *Samrock et al.* [2015] found no evidence for any deep (>5 km) low resistivity bodies that would be conventionally interpreted as an active magmatic system (i.e., a zone of partial melt) beneath Aluto. This finding appears to run in contrast to geological and geochemical observations
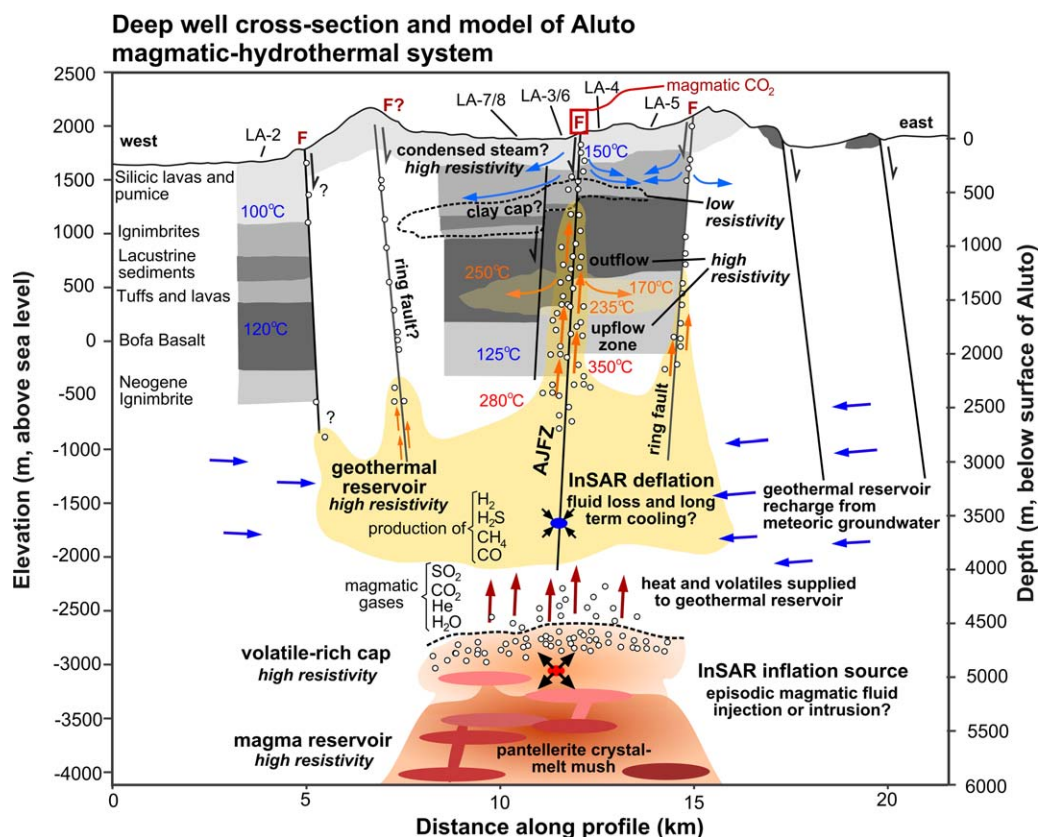
Figure 11. Schematic west-east cross section of the Aluto geothermal system. Deep stratigraphy and hypothesized subsurface structures on Aluto are summarized after *Hutchison et al.* [2015]. The deep stratigraphy summarizes results from several publications [*Gizaw*, 1993; *Gianelli and Teklemariam*, 1993; *Teklemariam et al.*, 1996] and drilling reports provided by the Geological Survey of Ethiopia [*Yimer*, 1984; *Mamo*, 1985; *ELC Electroconsult*, 1986; *Teklemariam*, 1996]. Red "F" labels indicate major fumarole and degassing regions mapped at the surface of the volcano [after *Hutchison et al.*, 2015]. The unit colors from light to dark gray provide a simple qualitative interpretation of permeability of the geological unit [after *Gizaw*, 1993]; the least permeable units are shown in darkest gray. Regions of high and low resistivity beneath Aluto were identified by magnetotelluric surveys and are identified in italics (for full details on absolute values the reader should refer to *Samrock et al.* [2015]). Our main interpretation is that the magmatic and hydrothermal reservoirs of Aluto are connected, and that magmatic volatiles are channelled to the surface by faults and fracture pathways.

from Aluto, e.g., the CO_2-$\delta^{13}C$ results, high CO_2 flux measurements (section 5), and young volcanism (<10 ka) [*Gianelli and Teklemariam*, 1993] which are all consistent with an active magmatic source that contributes significant volumes of volcanic gases and supplies melt for recent eruptions. An explanation that satisfies these apparently conflicting observations is that Aluto's magmatic system is represented by a locked crystal-rich mush rather than extensive zone of partial melt (as was imaged in the Dabbahu magmatic segment) [*Desissa et al.*, 2013]. It is important to recognize that there are have been few geophysical experiments to characterize peralkaline magmatic systems like Aluto and as a result our understanding of the relative volumes of partial melt, magmatic fluid and crystals in these systems, their interconnectivity and hence their detection thresholds is currently limited. We envisage a crystal-melt mush zone at ∼5–10 km to be the most plausible configuration of the magmatic system at Aluto; as has been suggested at other peralkaline systems in the EARS [e.g., *Macdonald et al.*, 2008]. Volatiles are transferred from the magmatic reservoir through fractures to the geothermal fluids, which then migrate along fault conduits to the surface where they boil and degas.

$\delta^{18}O$ measurements of waters extracted from the deep wells on Aluto reveal that the fluid contained within the geothermal reservoir is largely meteoric in origin (>90%); derived from rainfall on the rift margin [*Darling et al.*, 1996; *Rango et al.*, 2010]. Despite their proximity, the shallow lakes of Ziway, Langano, and Abijata supply minimal water (<10%) to the reservoir [*Darling et al.*, 1996]. Groundwater beneath Aluto flows toward the south, consistent with the hydraulic gradient, and hot spring discharges are focussed along the shore of Lake Langano [*Kebede et al.*, 1985; *Darling et al.*, 1996; *Rango et al.*, 2010; *Hutchison et al.*, 2015].

The subsurface structure of Aluto and lithological relationships (Figure 11) is constrained by data from the deep exploration wells [*Gizaw*, 1993; *Gianelli and Teklemariam*, 1993; *Teklemariam et al.*, 1996]. From well temperature and pressure measurements, these authors infer that the geothermal reservoir is >2000 m beneath the surface, and this is supported by magnetotelluric results [*Samrock et al.*, 2015] that confirm the presence of a high resistivity body at these depths. The main aquifer is likely to be a sequence of ignimbrites previously referred to as the "Tertiary" ignimbrites (now called Neogene ignimbrites, Figure 11). The reservoir fluids sampled from the deep wells are of alkali-chloride-bicarbonate type, with near-neutral pH, and display geochemical evidence for interaction with rhyolitic volcanic products [*Gianelli and Teklemariam*, 1993], consistent with the Neogene ignimbrite deposit (Figure 11) being the reservoir for the geothermal field.

Above the Neogene ignimbrites, a thick sequence of basalt lavas (Bofa Basalts) 500–1000 m thick are identified [*Teklemariam et al.*, 1996]. The basalts are pervasively altered and sealed by deposition of hydrothermal alteration minerals [e.g., *Gianelli and Teklemariam*, 1993; *Teklemariam et al.*, 1996]; as a result, they exhibit poor permeability [*Gizaw*, 1993]. Overlying the basalts, a layer of interbedded sediments and volcanic tuffs are encountered, these units are also highly altered and sealed by deposition of clay minerals [*Teklemariam et al.*, 1996]. This clay rich zone appears to correlate with a low-resistivity zone identified by *Samrock et al.* [2015] at depths of ∼500–1500 m (Figure 11). It is unclear whether the cap rock for the geothermal reservoir is made up by Bofa Basalt or the altered tuffs and sedimentary layers above. We consider that together the Bofa basalts and altered sediments-tuffs provide a capping lithology for the system (Figure 11, between 500 and 1500 m), although it is possible that the basalt unit serves as a reservoir along the contacts and where it is fractured and brecciated. Above the cap layers, peralkaline rhyolite volcanics erupted from the Aluto volcanic complex are encountered and comprise alternating layers of rhyolite lavas and volcaniclastic deposits. The ignimbrite at the base of these units (Figure 11) is permeable and appears to provide a cool shallow aquifer that has been identified in a number of the deep wells at <700 m [*Gizaw*, 1993].

The main feature of the Aluto geothermal field is that it is characterized by an upflow zone that coincides with the major NNE-trending AJFZ (Figures 2a and 10). Along this fault zone, the in-hole temperatures (in excess of 300°C), water chemistry (elevated Na/K ratios) [*Gizaw*, 1993], presence of high-temperature calc-silicate minerals (e.g., epidote, garnet, prehnite, tremolite-actinolite), and resistivity structure [*Samrock et al.*, 2015] all support upflow from the reservoir toward the surface. Temperature profiles from the bottom of these wells (∼2100 m) up to 700 m show this interval is characterized by boiling [*Gizaw*, 1993]. Either side of this zone of boiling lateral outflow of the reservoir fluid takes place. This is confirmed firstly, by temperature profiles in wells LA-4, LA-5, and LA-7 that show lower temperature (≤ 250°C) waters infiltrating at ∼1500 m (Figure 11), and second by water chemistry which shows the fluids are more concentrated and distinct from the reservoir fluid (i.e., waters have already boiled before entering the wells). Steam also condenses within the upflow zone and this likely supplies water to the cooler shallow (<700 m) aquifer (Figure 11) [*Gizaw*, 1993].

7. Causes of Unrest

Understanding the causes of unrest at calderas remains a key challenge in volcanology [*Acocella et al.*, 2015], and much of the debate focuses on discriminating between magmatic versus hydrothermal processes [e.g., *Lowenstern et al.*, 2006; *Gottsmann and Battaglia*, 2008; *Chiodini et al.*, 2012, 2015a]. Given our broad understanding of the geometry and connections between the magmatic and hydrothermal reservoirs (section 6, Figure 11) we now summarize our geodetic data and build a testable hypothesis for the causes of unrest at Aluto.

Ground surface displacement at Aluto is characterized by episodic accelerating uplift that causes edifice-wide inflation, followed initially by rapid subsidence and then slower deflation (section 4). The uplift location is roughly centered within the caldera and is constant through time (between 2004 and 2011, Figure 2). For the uplift, our analysis of the vertical and horizontal components of ground motion (Figure 6) and joint inversion of all InSAR observations (Figure 7) were consistent with a best-fitting spherical point source at a depth of ∼5.1 km beneath the surface. Since deep well observations place the main geothermal reservoir at a depth of >2 km (section 6), we infer that a ∼5 km inflation source is most likely located between the upper boundary of the magmatic reservoir and base of the geothermal system.

The uplift of active calderas is typically linked to fluid injection from depth into an inflating source region [*Pritchard and Simons*, 2002; *Wicks et al.*, 2006; *Parks et al.*, 2012, 2015]. At Aluto there is no evidence from any of the individual interferograms to suggest contracting sources elsewhere around the complex, so we infer that inflation was fed from a depth greater than 5 km. The uplift (inflation pulse) shows two steps, suggestive of an accelerating deformation trend (section 4.3, Figure 7d). This could either be explained by two pulses of fluid input to this source region [e.g., *Parks et al.*, 2015], or alternatively damage and fracturing, increasing permeability and allowing a greater rate of fluid supply. Deformation data alone do not allow us to investigate these possibilities, nor do they unambiguously differentiate between whether the fluid is gas, aqueous fluid, magma, or a combination of these. However, most peralkaline volcanoes are considered to have a volatile-rich cap at around 5–6 km depth [e.g., *Leat et al.*, 1984; *Mattia et al.*, 2007; *Biggs et al.*, 2009a; *Neave et al.*, 2012; *Macdonald et al.*, 2014]. This zone is consistent with our modeled source depth (Figure 7c) and our interpretation is that magmatic fluid injection or intrusions into this cap provide the source mechanism for uplift at Aluto (Figure 11).

At the point of peak uplift (maximum source inflation) subsidence (deflation) begins at Aluto (Figure 7d). A key feature of Aluto's deformation is the roll-over from uplift to subsidence which takes place over a timescale of a few months (section 4.3, Figure 7d). This short timescale is strongly suggestive of the migration of magmatic or hydrothermal fluids and degassing [e.g., *Todesco et al.*, 2004; *Wauthier et al.*, 2013; *Caricchi et al.*, 2014]. Ground subsidence is commonly observed during extraction of geothermal fluids [e.g., *Vasco et al.*, 2002, 2013; *Allis et al.*, 2009; *Keiding et al.*, 2010]. However, deformation related to commercial groundwater extraction is often spatially irregular, localized across a few subsidence peaks and most-importantly fault controlled [e.g., *Fialko and Simons*, 2000; *Vasco et al.*, 2002; *Samsonov et al.*, 2011; *Sarychikhina et al.*, 2011]. At Aluto, deflation patterns are caldera-wide (e.g., Figure 2f), analytical source models suggest deformation occurs at ∼3.5 km (Figure 6 and Table 2), and together this strongly suggests that fluids are being removed from deep within the geothermal reservoir.

Since our data suggest that the magmatic and hydrothermal reservoirs of Aluto are physically connected, our favored mechanism for the ground deformation at Aluto is that it represents a coupled magmatic-hydrothermal process. Our proposed mechanism involves uplift being caused by a fresh magmatic fluid pulse or intrusion into a shallow crustal reservoir at ∼5 km (Figure 11). As the inflating source region appears not to be well sealed, fluids and gas may then leak into the geothermal reservoir and ascend to the surface along fault pathways, leading to sharp deflation (Figure 7d). Slow long-term subsidence over the following years may reflect continued fluid loss and depressurization of the hydrothermal system consistent with the timescales predicted by numerical simulations of CO_2-rich magmatic fluid pulses [cf. *Chiodini et al.*, 2012].

Our hypothesis has many parallels with the suggestions made by *Samrock et al.* [2015] for causes of unrest at Aluto. Their interpretation is that unrest events are related to pulses of hot fluids entering the geothermal system and pose two physical mechanisms (clay swelling and thermoelastic expansion) that might be responsible. In their opinion, the apparent lack of a hot extended magma reservoir rules out a pure magmatic intrusion as the main cause of unrest. Together our new observations and the magnetotelluric results of *Samrock et al.* [2015] favor pulses of hot magmatic fluids entering a reservoir at ∼5 km as the root cause of uplift and subsequent fluid expulsion and degassing as the cause of subsidence.

To rigorously discriminate between whether a pulse of melt (i.e., a magmatic intrusion) or volatile fluids drive unrest would require a long-term monitoring protocol to be put in place at Aluto. For example, repeat geodetic and gravity surveys could be used to infer the density of the intrusive fluids and their relation to the deformation source [e.g., *Battaglia et al.*, 2003, 2006; *Gottsmann and Battaglia*, 2008; *Tizzani et al.*, 2009]. With these additional constraints on the subsurface and reservoir geometries increasingly complex and hence realistic source models could be considered for deformation analysis (e.g., finite spherical and ellipsoidal model [*McTigue*, 1987; *Yang et al.*, 1988] and also finite element models [*Masterlark et al.*, 2010; *Hickey et al.*, 2015]). Further, gas geochemical monitoring (e.g., He/CH_4 ratios [*Chiodini et al.*, 2015a] or repeat CO_2 surveys [*Parks et al.*, 2013]) could help confirm arrival of new magmatic gases at the surface, and when combined with geodetic observations, could reveal whether peak degassing follows maximum edifice inflation. Geochemical measurements and geophysical imaging need to be carried out across a period of unrest and should provide a much clearer understanding of how deep magmatic processes at Aluto transfer energy and fluids to the hydrothermal system, and how the major fault zones facilitate their release to the surface.

It is important to re-emphasize that comparable uplift-subsidence events are taking place at a number of caldera complexes in the EARS [*Biggs et al.*, 2009a, 2011, 2016], many of which are also being targeted for geothermal development. This provides an invaluable opportunity for government and geothermal industry stakeholders to put in place monitoring schemes that will ensure long-term safe, sustainable exploitation of the resources that these restless caldera systems host.

8. Conclusions

The Aluto magmatic and hydrothermal systems are physically connected by faults and fractures, such that deep (>2 km), hot (>250°C) geothermal fluids currently receive a continuous input of magmatic volatiles. Fluids migrate along areas of structural weakness, e.g., a proposed volcanic ring fault and major tectonic faults that dissect the complex, and ascend to the surface, releasing high-concentrations of magmatic CO_2 (δ^{13}C of -4.2‰ to -4.5‰). Episodic uplift-subsidence events typify the Aluto volcanic system and a joint inversion of new and existing InSAR data collected from 2008 to 2010 suggest that the uplift source is located at ∼5 km, and requires an inflationary volume change of ∼$+13 \times 10^6$ m^3. Uplift-subsidence events play out in a style that is characteristic of a coupled magmatic-hydrothermal system, and we propose that uplift is caused by a deep magmatic fluid injection or intrusion, and that faults provide key pathways for gas and fluid leakage into the geothermal reservoir. This hypothesis can be tested by monitoring changes in gas flux and composition along Aluto's main fault zone, which provides an important conduit for fluid upflow and sampling of these deeper reservoirs.

References

Abebe, B., V. Acocella, T. Korme, and D. Ayalew (2007), Quaternary faulting and volcanism in the Main Ethiopian Rift, *J. Afr. Earth Sci.*, *48*(2–3), 115–124, doi:10.1016/j.jafrearsci.2006.10.005.

Acocella, V., T. Korme, F. Salvini, and R. Funiciello (2003), Elliptic calderas in the Ethiopian Rift: Control of pre-existing structures, *J. Volcanol. Geotherm. Res.*, *119*, 189–203, doi:10.1016/S0377-0273(02)00342-6.

Acocella, V., R. Di Lorenzo, C. Newhall, and R. Scandone (2015), An overview of recent (1988 to 2014) caldera unrest: Knowledge and perspectives, *Rev. Geophys.*, *53*, 896–955, doi:10.1002/2015RG000492.

Agostini, A., M. Bonini, G. Corti, F. Sani, and F. Mazzarini (2011), Fault architecture in the Main Ethiopian Rift and comparison with experimental models: Implications for rift evolution and Nubia-Somalia kinematics, *Earth Planet. Sci. Lett.*, *301*(3–4), 479–492, doi:10.1016/j.epsl.2010.11.024.

Agusto, M., F. Tassi, A. T. Caselli, O. Vaselli, D. Rouwet, B. Capaccioni, S. Caliro, G. Chiodini, and T. Darrah (2013), Gas geochemistry of the magmatic-hydrothermal fluid reservoir in the Copahue-Caviahue volcanic complex (Argentina), *J. Volcanol. Geotherm. Res.*, *257*, 44–56, doi:10.1016/j.jvolgeores.2013.03.003.

Allis, R., C. Bromley, and S. Currie (2009), Update on subsidence at the Wairakei-Tauhara geothermal system, New Zealand, *Geothermics*, *38*(1), 169–180, doi:10.1016/j.geothermics.2008.12.006.

Barry, P. H., D. R. Hilton, T. P. Fischer, J. M. de Moor, F. Mangasini, and C. Ramirez (2013), Helium and carbon isotope systematics of cold "mazuku" CO_2 vents and hydrothermal gases and fluids from Rungwe Volcanic Province, southern Tanzania, *Chem. Geol.*, *339*(July), 141–156, doi:10.1016/j.chemgeo.2012.07.003.

Barry, P. H., D. R. Hilton, E. Füri, S. A. Halldórsson, and K. Grönvold (2014), Carbon isotope and abundance systematics of Icelandic geothermal gases, fluids and subglacial basalts with implications for mantle plume-related CO_2 fluxes, *Geochim. Cosmochim. Acta*, *134*, 74–99, doi:10.1016/j.gca.2014.02.038.

Battaglia, M., P. Segall, and C. Roberts (2003), The mechanics of unrest at Long Valley caldera, California. 2. Constraining the nature of the source using geodetic and micro-gravity data, *J. Volcanol. Geotherm. Res.*, *127*(3), 219–245, doi:10.1016/S0377-0273(03)00171-9.

Battaglia, M., C. Troise, F. Obrizzo, F. Pingue, and G. De Natale (2006), Evidence for fluid migration as the source of deformation at Campi Flegrei caldera (Italy), *Geophys. Res. Lett.*, *33*, L01307, doi:10.1029/2005GL024904.

Berardino, P., G. Fornaro, R. Lanari, and E. Sansosti (2002), A new algorithm for surface deformation monitoring based on small baseline differential SAR interferograms, *IEEE Trans. Geosci. Remote Sens.*, *40*(11), 2375–2383, doi:10.1109/IGARSS.2002.1025900.

Beutel, E., J. van Wijk, C. Ebinger, D. Keir, and A. Agostini (2010), Formation and stability of magmatic segments in the Main Ethiopian and Afar rifts, *Earth Planet. Sci. Lett.*, *293*(3–4), 225–235, doi:10.1016/j.epsl.2010.02.006.

Biggs, J., E. Y. Anthony, and C. J. Ebinger (2009a), Multiple inflation and deflation events at Kenyan volcanoes, East African Rift, *Geology*, *37*(11), 979–982, doi:10.1130/G30133A.1.

Biggs, J., D. P. Robinson, and T. H. Dixon (2009b), The 2007 Pisco, Peru, earthquake (M8.0): Seismology and geodesy, *Geophys. J. Int.*, *176*(3), 657–669, doi:10.1111/j.1365-246X.2008.03990.x.

Biggs, J., Z. Lu, T. Fournier, and J. T. Freymueller (2010), Magma flux at Okmok Volcano, Alaska, from a joint inversion of continuous GPS, campaign GPS, and interferometric synthetic aperture radar, *J. Geophys. Res.*, *115*, B12401, doi:10.1029/2010JB007577.

Biggs, J., I. D. Bastow, D. Keir, and E. Lewi (2011), Pulses of deformation reveal frequently recurring shallow magmatic activity beneath the Main Ethiopian Rift, *Geochem. Geophys. Geosyst.*, *12*, Q0AB10, doi:10.1029/2011GC003662.

Biggs, J., S. K. Ebmeier, W. P. Aspinall, Z. Lu, M. E. Pritchard, R. S. J. Sparks, and T. A. Mather (2014), Global link between deformation and volcanic eruption quantified by satellite imagery, *Nat. Commun.*, *5*, 3471–3471, doi:10.1038/ncomms4471.

Biggs, J., E. Robertson, and K. Cashman (2016), The lateral extent of volcanic interactions during unrest and eruption, *Nat. Geosci.*, *9*, 308–311, doi:10.1038/ngeo2658.

Boccaletti, M., M. Bonini, R. Mazzuoli, and B. Abebe (1998), Quaternary oblique extensional tectonics in the Ethiopian Rift (Horn of Africa), *Tectonophysics*, *287*, 97–116.

Bottinga, Y. (1969), Calculated fractionation factors for carbon and hydrogen isotope exchange in the system calcite-carbon dioxide-graphite-methane-hydrogen-water vapor, *Geochim. Cosmochim. Acta*, *33*(1), 49–64.

Brown, S. K., R. S. J. Sparks, K. Mee, C. Vye-Brown, E. Ilyinskaya, S. Jenkins, and S. C. Loughlin (2015), Regional and country profiles of volcanic hazard and risk. Report IV of the GVM/IAVCEI contribution to the Global Assessment Report on Disaster Risk Reduction 2015.

Caricchi, L., J. Biggs, C. Annen, and S. Ebmeier (2014), The influence of cooling, crystallisation and re-melting on the interpretation of geodetic signals in volcanic systems, *Earth Planet. Sci. Lett.*, *388*, 166–174, doi:10.1016/j.epsl.2013.12.002.

Casey, M., C. Ebinger, D. Keir, R. Gloaguen, and F. Mohamed (2006), Strain accommodation in transitional rifts: Extension by magma intrusion and faulting in Ethiopian rift magmatic segments, in *The Afar Volcanic Province within the East African Rift System*, edited by G. Yirgu, C. J. Ebinger, and P. K. H. Maguire, pp. 143–163, Geol. Soc. London Spec. Publ., doi:10.1144/GSL.SP.2006.259.01.13.

Cheng, W. (1996), Measurement of rhizosphere respiration and organic matter decomposition using natural ^{13}C, *Plant Soil*, *183*(2), 263–268.

Chiodini, G., R. Cioni, M. Guidi, and B. Raco (1998), Soil CO_2 flux measurements in volcanic and geothermal areas, *Appl. Geochem.*, *13*(5), 543–552.

Chiodini, G., S. Caliro, C. Cardellini, R. Avino, D. Granieri, and A. Schmidt (2008), Carbon isotopic composition of soil CO_2 efflux, a powerful method to discriminate different sources feeding soil CO_2 degassing in volcanic-hydrothermal areas, *Earth Planet. Sci. Lett.*, *274*(3–4), 372–379, doi:10.1016/j.epsl.2008.07.051.

Chiodini, G., S. Caliro, C. Cardellini, D. Granieri, R. Avino, A. Baldini, M. Donnini, and C. Minopoli (2010), Long-term variations of the Campi Flegrei, Italy, volcanic system as revealed by the monitoring of hydrothermal activity, *J. Geophys. Res.*, *115*, B03205, doi:10.1029/2008JB006258.

Chiodini, G., S. Caliro, P. De Martino, R. Avino, and F. Gherardi (2012), Early signals of new volcanic unrest at Campi Flegrei caldera? Insights from geochemical data and physical simulations, *Geology*, *40*(10), 943–946, doi:10.1130/G33251.1.

Chiodini, G., J. Vandemeulebrouck, S. Caliro, L. D'Auria, P. De Martino, A. Mangiacapra, and Z. Petrillo (2015a), Evidence of thermal-driven processes triggering the 2005–2014 unrest at Campi Flegrei caldera, *Earth Planet. Sci. Lett.*, *414*, 58–67, doi:10.1016/j.epsl.2015.01.012.

Chiodini, G., L. Pappalardo, A. Aiuppa, and S. Caliro (2015b), The geological CO_2 degassing history of a long-lived caldera, *Geology*, *43*, 767–770, doi:10.1130/G36905.1.

Cornwell, D. G., P. K. H. Maguire, R. W. England, and G. W. Stuart (2010), Imaging detailed crustal structure and magmatic intrusion across the Ethiopian Rift using a dense linear broadband array, *Geochem. Geophys. Geosyst.*, *11*, Q0AB03, doi:10.1029/2009GC002637.

Corti, G. (2009), Continental rift evolution: From rift initiation to incipient break-up in the Main Ethiopian Rift, East Africa, *Earth Sci. Rev.*, *96*(1–2), 1–53, doi:10.1016/j.earscirev.2009.06.005.

Corti, G., F. Sani, M. Philippon, D. Sokoutis, E. Willingshofer, and P. Molin (2013), Quaternary volcano-tectonic activity in the Soddo region, western margin of the Southern Main Ethiopian Rift, *Tectonics*, *32*, 861–879, doi:10.1002/tect.20052.

Darling, W. G. (1998), Hydrothermal hydrocarbon gases: 2. Application in the East African Rift system, *Appl. Geochem.*, *13*(7), 825–840.

Darling, W. G., E. Griesshaber, J. N. Andrews, H. Armannsson, and R. K. O'Nions (1995), The origin of hydrothermal and other gases in the Kenya Rift Valley, *Geochim. Cosmochim. Acta*, *59*(12), 2501–2512.

Darrah, T. H., D. Tedesco, F. Tassi, O. Vaselli, E. Cuoco, and R. J. Poreda (2013), Gas chemistry of the Dallol region of the Danakil Depression in the Afar region of the northern-most East African Rift, *Chem. Geol.*, *339*, 16–29, doi:10.1016/j.chemgeo.2012.10.036.

de Moor, J. M., T. P. Fischer, Z. D. Sharp, D. R. Hilton, P. H. Barry, F. Mangasini, and C. Ramirez (2013a), Gas chemistry and nitrogen isotope compositions of cold mantle gases from Rungwe Volcanic Province, southern Tanzania, *Chem. Geol.*, *339*, 30–42, doi:10.1016/j.chemgeo.2012.08.004.

Desissa, M., N. E. Johnson, K. A. Whaler, S. Hautot, S. Fisseha, and G. J. K. Dawes (2013), A mantle magma reservoir beneath an incipient mid-ocean ridge in Afar, Ethiopia, *Nat. Geosci.*, *6*(10), 861–865, doi:10.1038/ngeo1925.

Di Paola, G. M. (1972), The Ethiopian Rift Valley (between 7°00′ and 8°40′ lat. North), *Bull. Volcanol.*, *36*, 517–560.

Dvorak, J. J., and D. Dzurisin (1997), Volcano geodesy: The search for magma reservoirs and the formation of eruptive vents, *Rev. Geophys.*, *35*(3), 343–384.

Ebinger, C. (2005), Continental break-up: the East African perspective, *Astron. Geophys.*, *46*(April), 2.16–2.21.

Ebinger, C. J., and M. Casey (2001), Continental breakup in magmatic provinces: An Ethiopian example, *Geology*, *29*(6), 527–530, doi:10.1130/0091-7613(2001)029<0527:CBIMPA>2.0.CO;2.

Ebinger, C., A. Ayele, D. Keir, J. Rowland, G. Yirgu, T. Wright, M. Belachew, and I. Hamling (2010), Length and timescales of rift faulting and magma intrusion: The afar rifting cycle from 2005 to present, *Annu. Rev. Earth Planet. Sci.*, *38*(1), 439–466, doi:10.1146/annurev-earth-040809-152333.

Ebmeier, S. K., J. Biggs, T. A. Mather, G. Wadge, and F. Amelung (2010), Steady downslope movement on the western flank of Arenal volcano, Costa Rica, *Geochem. Geophys. Geosyst.*, *11*, Q12004, doi:10.1029/2010GC003263.

Ebmeier, S. K., J. Biggs, T. A. Mather, and F. Amelung (2013a), Applicability of InSAR to tropical volcanoes: Insights from Central America, *Geol. Soc. London Spec. Publ.*, *380*(1), 15–37, doi:10.1144/SP380.2.

Ebmeier, S. K., J. Biggs, T. A. Mather, and F. Amelung (2013b), On the lack of InSAR observations of magmatic deformation at Central American volcanoes, *J. Geophys. Res. Solid Earth*, *118*, 2571–2585, doi:10.1002/jgrb.50195.

ELC Electroconsult (1986), Exploitation of Aluto-Langano geothermal resources feasibility report, *Geothermal Exploration Project*, 289 p., Ethiopian Lake District Rift: Milan, Italy, ELC Electroconsult.

Ferguson, D. J., J. Maclennan, I. D. Bastow, D. M. Pyle, S. M. Jones, D. Keir, J. D. Blundy, T. Plank, and G. Yirgu (2013), Melting during late-stage rifting in Afar is hot and deep, *Nature*, *499*(7456), 70–73, doi:10.1038/nature12292.

Fialko, Y., and M. Simons (2000), Deformation and seismicity in the Coso geothermal area, Inyo County, California: Observations and modeling using satellite radar interferometry, *J. Geophys. Res.*, *105*(B9), 21,781, doi:10.1029/2000JB900169.

Fialko, Y., Y. Khazan, and M. Simons (2001), Deformation due to a pressurized horizontal circular crack in an elastic half-space, with applications to volcano geodesy, *Geophys. J. Int.*, *146*(1), 181–190, doi:10.1046/j.1365-246X.2001.00452.x.

Gerlach, T. M., and B. E. Taylor (1990), Carbon isotope constraints on degassing of carbon dioxide from Kilauea Volcano, *Geochim. Cosmochim. Acta*, *54*(7), 2051–2058.

Gianelli, G., and M. Teklemariam (1993), Water-rock interaction processes in the Aluto-Langano geothermal field (Ethiopia), *J. Volcanol. Geotherm. Res.*, *56*, 429–445.

Gizaw, B. (1993), Aluto-Langano geothermal field, Ethiopian Rift Valley: Physical characteristics and the effects of gas on well performance, *Geothermics*, *22*(2), 101–116.

Gottsmann, J., and M. Battaglia (2008), Deciphering causes of unrest at explosive collapse calderas: Recent advances and future challenges of joint time-lapse gravimetric and ground deformation studies, *Dev. Volcanol.*, *10*, 417–446, doi:10.1016/S1871-644X(07)00012-5.

Hayward, N., and C. Ebinger (1996), Variations in the along-axis segmentation of the Afar Rift system, *Tectonics*, *15*(2), 244–257.

Hickey, J., J. Gottsmann, and P. Mothes (2015), Estimating volcanic deformation source parameters with a finite element inversion: The 2001–2002 unrest at Cotopaxi volcano, Ecuador, *J. Geophys. Res. Solid Earth*, *120*, 1473–1486, doi:10.1002/2014JB011731.

Hutchison, W., T. A. Mather, D. M. Pyle, J. Biggs, and G. Yirgu (2015), Structural controls on fluid pathways in an active rift system: A case study of the Aluto volcanic complex, *Geosphere*, (3), 1–21, doi:10.1130/GES01119.1.

Javoy, M., and F. Pineau (1991), The volatiles record of a "popping" rock from the Mid-Atlantic Ridge at 14 N: Chemical and isotopic composition of gas trapped in the vesicles, *Earth Planet. Sci. Lett.*, *107*(3), 598–611.

Kebede, S. (2012), Geothermal exploration and development in Ethiopia: Status and future plan, in *Short Course VII on Exploration for Geothermal Resources Organized by UNU-GTP, GDC and KenGen*, 16 p., Lake Bogoria and Lake Naivasha, Kenya.

Kebede, S., T. Mamo, and T. Abebe (1985), *Geological report and explanation to the geological map of Aluto-Langano geothermal area*.

Keiding, M., T. Árnadóttir, S. Jónsson, J. Decriem, and A. Hooper (2010), Plate boundary deformation and man-made subsidence around geothermal fields on the Reykjanes Peninsula, Iceland, *J. Volcanol. Geotherm. Res.*, *194*(4), 139–149, doi:10.1016/j.jvolgeores.2010.04.011.

Keir, D., I. D. Bastow, G. Corti, F. Mazzarini, and T. O. Rooney (2015), The origin of along-rift variations in faulting and magmatism in the Ethiopian Rift, *Tectonics*, *34*(3), 464–477, doi:10.1002/2014TC003698.

Le Turdu, C., et al. (1999), The Ziway-Shala lake basin system, Main Ethiopian Rift: Influence of volcanism, tectonics, and climatic forcing on basin formation and sedimentation, *Palaeogeogr. Palaeoclimatol. Palaeoecol.*, *150*(3–4), 135–177, doi:10.1016/S0031-0182(98)00220-X.

Leat, P. T., R. MacDonald, and R. L. Smith (1984), Geochemical evolution of the Menengai Caldera Volcano, Kenya, *J. Geophys. Res. Solid Earth*, *89*(B10), 8571–8592, doi:10.1029/JB089iB10p08571.

Lee, H., J. D. Muirhead, T. P. Fischer, C. J. Ebinger, S. A. Kattenhorn, Z. D. Sharp, and G. Kianji (2016), Massive and prolonged deep carbon emissions associated with continental rifting, *Nat. Geosci.*, *9*, 145–149, doi:10.1038/ngeo2622.

Lollar, B. S., C. J. Ballentine, and R. K. Onions (1997), The fate of mantle-derived carbon in a continental sedimentary basin: Integration of CHe relationships and stable isotope signatures, *Geochim. Cosmochim. Acta*, *61*(11), 2295–2307.

Lowenstern, J. B., R. B. Smith, and D. P. Hill (2006), Monitoring super-volcanoes: Geophysical and geochemical signals at Yellowstone and other large caldera systems, *Philos. Trans. R. Soc. A*, *364*(1845), 2055–2072, doi:10.1098/rsta.2006.1813

Lundgren, P., S. Usai, E. Sansosti, R. Lanari, M. Tesauro, G. Fornaro, and P. Berardino (2001), Modeling surface deformation observed with synthetic aperture radar interferometry at Campi Flegrei caldera, *J. Geophys. Res.*, *106*(B9), 2001, doi:10.1029/2001JB000194.

Macdonald, R., H. E. Belkin, J. G. Fitton, N. W. Rogers, K. Nejbert, A. G. Tindle, and A. S. Marshall (2008), The roles of fractional crystallization, magma mixing, crystal mush remobilization and volatile-melt interactions in the genesis of a Young Basalt-peralkaline rhyolite suite, the Greater Olkaria volcanic complex, Kenya Rift Valley, *J. Petrol.*, *49*(8), 1515–1547, doi:10.1093/petrology/egn036.

Macdonald, R., B. Bagiński, and B. G. J. Upton (2014), The volcano-pluton interface; the Longonot (Kenya) and Kûngnât (Greenland) peralkaline complexes, *Lithos*, *196*, 232–241, doi:10.1016/j.lithos.2014.03.009.

Macpherson, C., and D. Mattey (1994), Carbon isotope variations of CO_2 in Central Lau Basin basalts and ferrobasalts, *Earth Planet. Sci. Lett.*, *121*(3), 263–276.

Mamo, T. (1985), *Petrography and rock chemistry of well LA-8 Aluto-Langano geothermal system, Ethiopia, Unpublished report*, Geothermal Institute, Univ. of Auckland, 48 pp.

Mann, D., and J. T. Freymueller (2003), Volcanic and tectonic deformation on Unimak Island in the Aleutian Arc, Alaska, *J. Geophys. Res.*, *108*(B2), 2108, doi:10.1029/2002JB001925.

Masterlark, T., M. Haney, H. Dickinson, T. Fournier, and C. Searcy (2010), Rheologic and structural controls on the deformation of Okmok volcano, Alaska: FEMs, InSAR, and ambient noise tomography, *J. Geophys. Res.*, *115*, B02409, doi:10.1029/2009JB006324.

McTigue, D. F. (1987), Elastic stress and deformation near a finite spherical magma body: Resolution of the point source paradox, *J. Geophys. Res.*, *92*(B12), 12,931–12,940, doi:10.1029/JB092iB12p12931.

Mattia, M., A. Bonaccorso, and F. Guglielmino (2007), Ground deformations in the Island of Pantelleria (Italy): Insights into the dynamic of the current intereruptive period, *J. Geophys. Res*, *112*, B11406, doi:10.1029/2006JB004781.

Mogi, K. (1958), Relations between the eruptions of various volcanoes and the deformations of the ground surfaces around them, *Bull. Earthquake Res. Inst. Univ. Tokyo*, *36*, 99–134.

Mohr, P., J. G. Mitchell, and R. G. H. Raynolds (1980), Quaternary volcanism and faulting at O'A caldera, Central Ethiopian Rift, *Bull. Volcanol.*, *43*(1), 173–189, doi:10.1007/BF02597619.

Mook, W. G., J. C. Bommerson, and W. H. Staverman (1974), Carbon isotope fractionation between dissolved bicarbonate and gaseous carbon dioxide, *Earth Planet. Sci. Lett.*, *22*(2), 169–176.

Moore, R. K., J. P. Claassen, and Y. H. Lin (1981), Scanning spaceborne synthetic aperture radar with integrated radiometer, *IEEE Trans. Aerosp. Electron. Syst.*, *AES-17*(3), 410–421.

Neave, D. A., G. Fabbro, R. A. Herd, C. M. Petrone, and M. Edmonds (2012), Melting, differentiation and degassing at the Pantelleria Volcano, Italy, *J. Petrol.*, *53*(3), 637–663, doi:10.1093/petrology/egr074.

Parks, M. M., et al. (2012), Evolution of Santorini Volcano dominated by episodic and rapid fluxes of melt from depth, *Nat. Geosci.*, *5*(10), 749–754, doi:10.1038/ngeo1562.

Parks, M. M., S. Caliro, G. Chiodini, D. M. Pyle, T. A. Mather, K. Berlo, M. Edmonds, J. Biggs, P. Nomikou, and C. Raptakis (2013), Distinguishing contributions to diffuse CO_2 emissions in volcanic areas from magmatic degassing and thermal decarbonation using soil gas ^{222}Rn-δ^{13}C systematics: Application to Santorini volcano, Greece, *Earth Planet. Sci. Lett.*, *377*–378, 180–190, doi:10.1016/j.epsl.2013.06.046.

Parks, M. M., J. D. P. Moore, X. Papanikolaou, J. Biggs, T. A. Mather, D. M. Pyle, C. Raptakis, D. Paradissis, A. Hooper, and B. Parsons (2015), From quiescence to unrest: 20 years of satellite geodetic measurements at Santorini volcano, Greece, *J. Geophys. Res. Solid Earth*, *120*, 1309–1328, doi:10.1002/2014JB011540.

Philippon, M., G. Corti, F. Sani, M. Bonini, M. Balestrieri, P. Molin, E. Willingshofer, D. Sokoutis, and S. Cloetingh (2014), Evolution, distribution, and characteristics of rifting in southern Ethiopia, *Tectonics*, *33*(4), 485–508, doi:10.1002/2013TC003430.

Pritchard, M. E., and M. Simons (2002), A satellite geodetic survey of large-scale deformation of volcanic centres in the central Andes, *Nature*, *418*(6894), 167–171, doi:10.1038/nature00872.

Rampey, M. L., C. Oppenheimer, D. M. Pyle, and G. Yirgu (2010), Caldera-forming eruptions of the Quaternary Kone volcanic complex, Ethiopia, *J. Afr. Earth Sci.*, *58*(1), 51–66, doi:10.1016/j.jafrearsci.2010.01.008.

Rampey, M. L., C. Oppenheimer, D. M. Pyle, and G. Yirgu (2014), Journal of African Earth Sciences Physical volcanology of the Gubisa Formation, Kone volcanic complex, Ethiopia, *J. Afr. Earth Sci.*, *96*, 212–219, doi:10.1016/j.jafrearsci.2014.04.009.

Rango, T., R. Petrini, B. Stenni, G. Bianchini, F. Slejko, L. Beccaluva, and T. Ayenew (2010), The dynamics of central Main Ethiopian Rift waters: Evidence from δD, δ^{18}O and ^{87}Sr/^{86}Sr ratios, *Appl. Geochem.*, *25*(12), 1860–1871, doi:10.1016/j.apgeochem.2010.10.001.

Robertson, E. A. M., J. Biggs, K. V Cashman, M. A. Floyd, and C. Vye-Brown (2015), Influence of regional tectonics and pre-existing structures on the formation of elliptical calderas in the Kenyan Rift, *Geol. Soc. London Spec. Publ. 420*, SP420-12, doi:10.1144/SP420.12.

Rooney, T. O., I. D. Bastow, and D. Keir (2011), Insights into extensional processes during magma assisted rifting: Evidence from aligned scoria cones, *J. Volcanol. Geotherm. Res., 201*(1–4), 83–96, doi:10.1016/j.jvolgeores.2010.07.019.

Rosen, P. A., S. Hensley, G. Peltzer, and M. Simons (2004), Updated repeat orbit interferometry package released, *Eos Trans. AGU, 85*(5), 47.

Samrock, F., A. Kuvshinov, J. Bakker, A. Jackson, and S. Fisseha (2015), 3-D analysis and interpretation of magnetotelluric data from the Aluto-Langano geothermal field, Ethiopia, *Geophys. J. Int., 202*(3), 1923–1948, doi:10.1093/gji/ggv270.

Samsonov, S., J. Beavan, P. J. González, K. Tiampo, and J. Fernández (2011), Ground deformation in the Taupo Volcanic Zone, New Zealand, observed by ALOS PALSAR interferometry, *Geophys. J. Int., 187*(1), 147–160, doi:10.1111/j.1365-246X.2011.05129.x.

Sano, Y., and B. Marty (1995), Origin of carbon in fumarolic gas from island arcs, *Chem. Geol., 119*(1), 265–274.

Saria, E., E. Calais, D. S. Stamps, D. Delvaux, and C. J. H. Hartnady (2014), Present-day kinematics of the East African Rift, *J. Geophys. Res. Solid Earth, 119*, 3584–3600, doi:10.1002/2013JB010901.

Sarychikhina, O., E. Glowacka, R. Mellors, and F. S. Vidal (2011), Land subsidence in the Cerro Prieto Geothermal Field, Baja California, Mexico, from 1994 to 2005: An integrated analysis of DInSAR, leveling and geological data, *J. Volcanol. Geotherm. Res., 204*(1), 76–90, doi: 10.1016/j.jvolgeores.2011.03.004.

Siebert, L., and T. Simkin (2002), Volcanoes of the World: An Illustrated Catalog of Holocene Volcanoes and their Eruptions, Smithsonian Institution, *Global Volcanism Program Digital Information Series, GVP-3.* [Available at http://www.volcano.si.edu.]

Sigmundsson, F., S. Hreinsdóttir, A. Hooper, T. Árnadóttir, R. Pedersen, M. J. Roberts, N. Óskarsson, A. Auriac, J. Decriem, and P. Einarsson (2010), Intrusion triggering of the 2010 Eyjafjallajokull explosive eruption, *Nature, 468*, 426–430, doi:10.1038/nature09558.

Sigmundsson, F., A. Hooper, S. Hreinsdóttir, K. S. Vogfjörd, B. G. Ófeigsson, E. R. Heimisson, S. Dumont, M. Parks, K. Spaans, and G. B. Gudmundsson (2014), Segmented lateral dyke growth in a rifting event at Bardarbunga volcanic system, Iceland, *Nature, 517*, 191–195, doi:10.1038/nature14111.

Simons, M., and P. A. Rosen (2007) Interferometric synthetic aperture radar geodesy, in *Treatise on Geophysics—Geodesy*, vol. 3, pp. 391–446, Elsevier, Amsterdam.

Szaran, J. (1997), Achievement of carbon isotope equilibrium in the system HCO_3-(solution)-CO_2 (gas), *Chem. Geol., 142*(1), 79–86.

Tassi, F., F. Aguilera, T. Darrah, O. Vaselli, B. Capaccioni, R. J. Poreda, and A. D. Huertas (2010), Fluid geochemistry of hydrothermal systems in the Arica-Parinacota, Tarapacá and Antofagasta regions (northern Chile), *J. Volcanol. Geotherm. Res., 192*(1), 1–15, doi:10.1016/j.jvolgeores.2010.02.006.

Tassi, F., O. Vaselli, C. B. Papazachos, L. Giannini, G. Chiodini, G. E. Vougioukalakis, E. Karagianni, D. Vamvakaris, and D. Panagiotopoulos (2013), Geochemical and isotopic changes in the fumarolic and submerged gas discharges during the 2011-2012 unrest at Santorini caldera (Greece), *Bull. Volcanol., 75*, 1–15, doi:10.1007/s00445-013-0711-8.

Tedesco, D., F. Tassi, O. Vaselli, R. J. Poreda, T. Darrah, E. Cuoco, and M. M. Yalire (2010), Gas isotopic signatures (He, C, and Ar) in the Lake Kivu region (western branch of the East African rift system): Geodynamic and volcanological implications, *J. Geophys. Res., 115*, B01205, doi:10.1029/2008JB006227.

Teklemariam, M. (1996), Water-rock interaction processes in the Aluto-Langano geothermal field Ethiopia, Unpublished PhD thesis, 245 pp., Univ. of Pisa.

Teklemariam, M., S. Battaglia, G. Gianelli, and G. Ruggieri (1996), Hydrothermal alteration in the Aluto-Langano geothermal field, Ethiopia, *Geothermics, 25*(6), 679–702.

Tizzani, P., M. Battaglia, G. Zeni, S. Atzori, P. Berardino, and R. Lanari (2009), Uplift and magma intrusion at Long Valley caldera from InSAR and gravity measurements, *Geology, 37*(1), 63–66, doi:10.1130/G25318A.1.

Todesco, M., J. Rutqvist, G. Chiodini, K. Pruess, and C. M. Oldenburg (2004), Modeling of recent volcanic episodes at Phlegrean Fields (Italy): Geochemical variations and ground deformation, *Geothermics, 33*(4), 531–547, doi:10.1016/j.geothermics.2003.08.014.

Tu, K. P., P. D. Brooks, and T. E. Dawson (2001), Using septum-capped vials with continuous-flow isotope ratio mass spectrometric analysis of atmospheric CO_2 for Keeling plot applications, *Rapid Commun. Mass Spectrom., 15*(12), 952–956, doi:10.1002/rcm.320.

Vasco, D. W., C. Wicks, K. Karasaki, and O. Marques (2002), Geodetic imaging: Reservoir monitoring using satellite interferometry, *Geophys. J. Int., 149*(3), 555–571, doi:10.1046/j.1365-246X.2002.01569.x.

Vasco, D. W., J. Rutqvist, A. Ferretti, A. Rucci, F. Bellotti, P. Dobson, C. Oldenburg, J. Garcia, M. Walters, and C. Hartline (2013), Monitoring deformation at the Geysers Geothermal Field, California using C-band and X-band interferometric synthetic aperture radar, *Geophys. Res. Lett., 40*, 2567–2572, doi:10.1002/grl.50314.

Vogel, J. C., P. M. Grootes, and W. G. Mook (1970), Isotopic fractionation between gaseous and dissolved carbon dioxide, *Z. Phys., 230*(3), 225–238.

Wauthier, C., V. Cayol, F. Kervyn, and N. d'Oreye (2012), Magma sources involved in the 2002 Nyiragongo eruption, as inferred from an InSAR analysis, *J. Geophys. Res., 117*, B05411, doi:10.1029/2011JB008257.

Wauthier, C., V. Cayol, M. Poland, F. Kervyn, N. d'Oreye, A. Hooper, S. Samsonov, K. Tiampo, and B. Smets (2013), Nyamulagira's magma plumbing system inferred from 15 years of InSAR, *Geol. Soc. London Spec. Publ., 380*(1), 39–65, doi:10.1144/SP380.9.

Weaver, S. D., J. S. C. Sceal, and I. L. Gibson (1972), Trace-element data relevant to the origin of trachytic and pantelleritic lavas in the East African Rift system, *Contrib. Mineral. Petrol., 36*(3), 181–194, doi:10.1007/BF00371430.

Wegmüller, U., and C. Werner (1997), Gamma SAR processor and interferometry software, *ESA SP*, 1687–1692.

Wicks, C. W., W. Thatcher, D. Dzurisin, and J. Svarc (2006), Uplift, thermal unrest and magma intrusion at Yellowstone caldera, *Nature, 440*(7080), 72–75, doi:10.1038/nature04507.

Wright, T. J., B. E. Parsons, and Z. Lu (2004), Toward mapping surface deformation in three dimensions using InSAR, *Geophys. Res. Lett., 31*, L01607, doi:10.1029/2003GL018827.

Wright, T. J., C. Ebinger, J. Biggs, A. Ayele, G. Yirgu, D. Keir, and A. Stork (2006), Magma-maintained rift segmentation at continental rupture in the 2005 Afar dyking episode, *Nature, 442*(7100), 291–294, doi:10.1038/nature04978.

Yang, X., P. M. Davis, and J. H. Dieterich (1988), Deformation from inflation of a dipping finite prolate spheroid in an elastic half-space as a model for volcanic stressing, *J. Geophys. Res., 93*(B5), 4249–4257, doi:10.1029/JB093iB05p04249.

Yimer, M. (1984), The petrogenesis, chemistry and hydrothermal mineralogy of rocks in the Langano-Aluto geothemal system, Ethiopia, Unpublished report, Geothermal Institute, *University of Auckland*, 75 pp., Geotherm. Inst., Univ. of Auckland, New Zealand.

Younger, P. L. (2014), Missing a trick in geothermal exploration, *Nat. Geosci., 7*(7), 479–480, doi:10.1038/ngeo2193.